Effect of Density Gradients in Confined Supersonic Shear Layers

Oshin Peroomian and R.E. Kelly
Mechanical Aerospace and Nuclear Engineering Department, University of California at Los Angeles, Los Angeles, California, 90024

The effect of density gradients on the supersonic wall modes (acoustic modes) of a 2-D confined compressible shear layer were investigated using linear analysis. Due to the inadequacies of the hyperbolic tangent profile, the boundary layer basic profiles were used. First a test case was taken with the same parameters as in Tam and Hu's[15] analysis with convective Mach number $M_c = 1.836$ and density ratio of 1.398. Three generalized inflection points were found giving rise to three modes. The first two show similar properties to the Class A and B modes in Ref. 15, and the third is an 'inner mode' which will be called a Class C mode. As the density ratio is increased, the smallest of the three neutral phase speeds tends towards the speed of the lower velocity stream, and the other two eventually coalesce and then disappear. These two effects lead to a linear resonance between the Class B modes which increases the cutoff frequency and growth rate of the lowest mode. In fact, growth rates of 2-4 times the test case were found as the density ratio was increased to 7. A similar trend is observed for the Class A modes when the density ratio is

decreased from the test case, but the growth rate is not changed by much from the test case.

I. Introduction

The study of compressible shear layers has been thrust into the spotlight in the past decade mainly due to the need for supersonic combustors (SCRAM-JETS) in future generation aircraft. Numerous analyses have been conducted in order to better understand the instability characteristics and dynamics of compressible shear layers. In what follows a brief overview of some of these analyses will be presented with emphasis on work done using linear analysis. In the overview the term 'constant density' will refer to cases when the density and temperature of the basic flow are taken to be constant throughout the shear layer so that their variation in the shear layer due to viscous heating is ignored. The researchers who have included viscous heating effects have used either the Busemann-Crocco (B-C) relations or some solution of the boundary layer equations for the density and temperature profiles.

Some early work done on the inviscid instability of compressible shear layers was reported in a series of papers by Blumen[1], Blumen *et al.*[2] and Drazin and Garvey[3]. The work involved a 2-D temporal linear stability analysis of a compressible, constant density, unbounded shear layer modeled by a hyperbolic tangent profile based on the cross-stream coordinate, with equal and opposite velocities at the ends. For subsonic Mach numbers, they found a single mode

whose growth rate decreased as the Mach number increased. This mode is a Kelvin-Helmholtz (K-H) type of instability similar to that occurring in incompressible shear layers. As the Mach number is increased, the first order effect of compressibility is to decrease the growth rate of the 2-D K-H mode. For supersonic Mach numbers, two modes were found with equal but opposite phase speeds. These modes had very small growth rates compared to the subsonic K-H mode. Jackson and Grosch[4] conducted a spatial stability analysis of a compressible shear layer (lower stream was quiescent) modeled by a hyperbolic tangent profile whose independent variable was a similarity variable based on Howarth's transformation. Since this similarity variable is dependent on the Mach number, the hyperbolic tangent profile based on this transformation is also dependent on the Mach number. They computed the neutral modes for 2-D and 3-D disturbances and also found two modes for supersonic Mach numbers. One mode was supersonic with respect to the slow stream and subsonic with respect to the fast stream and was called a 'fast mode'. The other was supersonic with respect to the fast stream and subsonic with respect to the slow stream and was called a 'slow mode'. These modes were characterized by Mack[5] as radiating vorticity modes because of the oscillatory behavior of the eigenfunctions outside the shear layer. Sandham and Reynolds[6,7] independently confirmed the existence of these modes using a profile based on the

similarity solution of the compressible boundary layer equations. They also showed that for convective Mach numbers (M_c), i.e. Mach number relative to the phase speed of the instability, above a critical subsonic value the most unstable disturbances were three-dimensional. This is in clear contrast to the incompressible case. Similar results were obtained earlier by Gropengiesser[8] and Lessen *et al.*[9,10]. Other studies on the unbounded compressible shear layer were conducted by Ragab and Wu[11,12,13], with the latter two references dealing with subharmonic instabilities in this type of shear layer.

For later reference, it is also necessary to mention some results obtained by researchers concerning the use of the different profiles used for the above analyses. Sandham and Reynolds[6] showed that use of the hyperbolic tangent profile based on the cross-steam coordinate was unsatisfactory for cases of high shear or density ratio even at very low Mach numbers. They showed that errors of up to 16% in the growth rates can exist relative to the growth rates obtained by use of the boundary layer profiles. Jackson and Grosch[14] used three different profiles in investigating the fast and slow modes in a spatial shear layer. The first was a hyperbolic tangent profile based on the similarity variable mentioned above, the second was a profile based on the similarity solutions of the boundary layer profiles with a linear viscosity law and Prandtl number (Pr) equal to 1.0, and the third was a similar profile but with the

Sutherland viscosity law incorporated and $Pr = 0.7$. They showed that the results obtained by using the first profile were only qualitatively similar to the ones from the other two profiles.

The analyses which more closely pertain to the current research were done on bounded (confined) shear layers as shown in Figure 1. Tam and Hu[15] and Greenough *et al.*[16] conducted spatial and temporal analyses for a bounded shear layer. Greenough *et. al* used a hyperbolic tangent profile based on the cross-stream coordinate and only considered the constant density case. They also found a single mode for subsonic Mach numbers. However, multiple modes were found when the Mach number was supersonic. These modes are different from the radiating vorticity modes found in the unbounded shear layer and were referred to as supersonic wall modes by Greenough or acoustic modes by Mack[5]. Tam and Hu[15] conducted a thorough spatial analysis of these modes using both a hyperbolic tangent profile (based on the cross-stream coordinate and using the B-C relations) as well as a vortex sheet model. For the vortex sheet model, they found two families of instability modes and labeled them Class A and Class B modes. They also found two families of neutral modes which they label Class C and D acoustic neutral modes. For the finite shear layer case, only the unstable solutions were shown because the contour of integration was not deflected in their analysis to avoid the critical layer.[17]

Tam and Hu found that for a relatively thick shear layer the most unstable mode is the first Class A 2-D mode. Mack[5] discussed in detail the nature of these acoustic modes as they pertain to boundary layers, wakes, jets and confined shear layers. The underlying condition which needs to exist in order for acoustic modes to be observed is a region of trapped supersonic flow relative to the phase speed of the instability wave. This means that either two sonic lines ($M_c = 1.0$), two walls or a combination of the two must exist in the flow. More results and facts about Tam and Hu's analysis are given in the body of the present paper since they are needed for comparison to our own results.

The effects of walls on the instabilities occurring in compressible shear layers were investigated by Zhuang *et al.*[18] and Morris *et al.*[19]. They showed results indicating that the subsonic mode was not affected by the walls as long as the walls were not too close (10 vorticity thicknesses away). They also showed that, as the walls were brought in from infinity the radiating vorticity modes for supersonic Mach numbers first decreased in growth rate and then disappeared. Meanwhile, a new set of modes, which were not continuations of the vorticity modes, appeared and dominated the 2-D disturbances.

There have been numerous numerical simulations done on unbounded shear layers such as Lele[20], Sandham and Reynolds[6,7], Ragab and Wu[13], and Ragab and Sheen[21] confirming the results obtained from linear analysis. Some have

also considered the bounded shear layer in their numerical simulations, such as Greenough *et al.*, Sigalla *et al.*[22,23], Huang and Riley[24], Lu and Wu[25,26] and Gathmann *et al.*[27].

Many experiments have been conducted on the instability of shear layers, one of the most famous experiments being done by Brown and Roshko[28]for very low subsonic Mach numbers. They showed the existence of large scale coherent structures which were formed within the shear layer and also showed that the growth of the shear layer depended linearly on the velocity ratio parameter ($\frac{U_1-U_2}{U_1+U_2}$). They also looked at the effect of density ratio on the growth of the shear layer by taking three points ($\frac{\rho_2}{\rho_1} = 7, 1, \frac{1}{7}$) and observed that when the density of the lower(slower) stream is greater than the upper(faster) stream the growth rate increases from the uniform density case. The opposite was true when the upper stream was heavier than the lower one. Recently experiments on the compressible mixing layer have been conducted by Papamoschou and Roshko[29,30]. They observed a reduction in growth rate as a function of Mach number. They also showed that the growth rate curves could be parameterized by the use of a single Mach number which they defined as the *Convective Mach Number* ,M_c. The definition of this Mach number is based upon using a reference frame associated with the dominant wave. They defined two convective Mach numbers:

$$M_{c1} = \frac{U_1 - U_c}{a_1} \tag{1.1}$$

and

$$M_{c2} = \frac{U_c - U_2}{a_2}, \tag{1.2}$$

where U_c is the speed of the dominant structure and a_1, a_2 are the speeds of sound in the two streams. By using an argument that the two streams share a common stagnation point, they showed that if the two streams have the same specific heat ratio then $M_{c1} = M_{c2}$. Also from these arguments, it follows that:

$$U_c = \frac{a_2 U_1 + a_1 U_2}{a_1 + a_2}, \tag{1.3}$$

and

$$M_c = \frac{U_1 - U_2}{a_1 + a_2}. \tag{1.4}$$

For small Mach numbers and almost equal specific heat ratios, they showed that one could express U_c in terms of the density ratio:

$$\frac{U_c}{U_1} = \frac{1 + \frac{U_2}{U_1}\left(\frac{\rho_2}{\rho_1}\right)^{\frac{1}{2}}}{1 + \left(\frac{\rho_2}{\rho_1}\right)^{\frac{1}{2}}} \tag{1.5}$$

Papamoschou[31] has recently given a revised version of the above model for the case when the Mach number is high enough to produce shocks within the flow. In these cases it was found that $M_{c1} \neq M_{c2}$, and so an asymmetric situation arises. This was predicted in the analysis of Jackson and Grosch[4] in regard to their slow and fast modes. (i.e. the supersonic modes don't obey the U_c formula given above even for the constant density case). Papamoschou gave a revised model accounting for shock formation in the stream which is supersonic with respect to the dominant structure. More will be said regarding this result obtained by Papamoschou in later sections. The concept of convective Mach number has been applied to linear analysis by replacing U_c, the speed of the dominant structure, by c_r, the phase speed of the instability.

In this paper, first the governing equations and solution procedures will be discussed. The profiles of the basic flow velocity and density will be calculated from the boundary layer equations rather than assumed as in Tam and Hu[15]. The results for a test case matching the parameters in Tam and Hu's analysis will then be presented. In the final portion, the results obtained when increasing and decreasing the density ratio from this test case will be

discussed.

II. Flow Model and Governing Equations

The model which is studied here is a confined compressible shear layer formed by two gases with different velocities, densities and properties, but with the same constant pressure. Figure 1 shows the configuration used in this analysis. The subscript 1 is used for the quantities related to the high speed freestream and the subscript 2 for the quantities of the low speed freestream. The streamwise coordinate is x, the spanwise coordinate is z, and the cross-stream coordinate is y. For simplicity, free slip wall boundary conditions are assumed at the walls of the channel. It is also assumed that the flow is inviscid, non-conducting, and non-diffusive. For this situation the governing equations are the Euler equations for a two species system and in dimensional form can be written as the following:

$$\frac{\partial \rho^*}{\partial t^*} + \nabla \cdot (\rho^* \vec{v}^*) = 0 \tag{2.1}$$

$$\rho^* (\frac{\partial \vec{v}^*}{\partial t^*} + \vec{v}^* \cdot \nabla \vec{v}^*) + \nabla p^* = 0 \tag{2.2}$$

$$\rho^*(\frac{\partial h^*}{\partial t^*} + \vec{v}^* \cdot \nabla h^*) - \frac{\partial p^*}{\partial t^*} - \vec{v}^* \cdot \nabla p^* = 0 \tag{2.3}$$

$$\frac{\partial C_a}{\partial t^*} + \vec{v}^* \cdot \nabla C_a = 0 \tag{2.4}$$

$$p^* = \rho^* R^* T^* \tag{2.5}$$

$$C_a = \frac{\rho_a^*}{\rho^*}, \quad C_b = \frac{\rho_b^*}{\rho^*}, \quad \rho^* = \rho_a^* + \rho_b^* \quad C_a + C_b = 1 \tag{2.6}$$

where ρ^* is the density of the gas mixture, T^* is the temperature, p^* is the pressure, $\vec{v}^*$ is the velocity vector, h^* is the enthalpy which can be related to the temperature by $h^* = [c_{p_a}^* C_a + c_{p_b}^*(1 - C_a)]T^*$ where $c_{p_a}^*$ and $c_{p_b}^*$ are the specific heat ratios at constant pressure, and C_a is the mass fraction (species concentration) of species a. Also, $R^* = [R_a^* C_a + R_b^*(1 - C_a)]$ is the gas constant of the mixture.

These equations are non-dimensionalized using the fast (upper) freestream quantities, ρ_1^*, U_1^*, T_1^* and the height of the channel, H^*. Thermodynamic properties are also non-dimensionalized by the upper freestream thermodynamic properties, $c_{p_a}^*$ and R_a^*. Based on this non-dimensionalization, the density ratio $\frac{\rho_2^*}{\rho_1^*}$ and the velocity ratio $\frac{U_2^*}{U_1^*}$ are defined as ρ_2 and U_2, respectively.

Once the equations are non-dimensionalized, they are linearized around a parallel basic flow $(\bar{\rho}(y), \bar{P}, \bar{U}(y), \bar{C}_a(y))$. These basic flow quantities can be found in several ways which will be discussed later. The flow variables can be written as:

$$\rho = \bar{\rho}(y) + \rho'(x, y, z, t) \tag{2.7a}$$

$$p = \bar{P} + p'(x, y, z, t) \tag{2.7b}$$

$$u = \bar{U}(y) + u'(x, y, z, t) \tag{2.7c}$$

$$v = v'(x, y, z, t) \tag{2.7d}$$

$$w = w'(x, y, z, t) \tag{2.7e}$$

$$T = \bar{T}(y) + T'(x, y, z, t) \tag{2.7f}$$

$$C_a = \bar{C}_a(y) + c_a'(x, y, z, t) \tag{2.7g}$$

Normal modes are assumed for these infinitesimal disturbances with the form:

$$q' = \hat{q}(y)\, exp[i(kx + \beta z - \omega t)] \tag{2.8}$$

where $\hat{q}$ is the eigenfunction, k and β are the streamwise and spanwise wave numbers and ω is the frequency. In general k, β and ω are complex. Once these normal modes are substituted into the equations of motion, a single O.D.E. can be found for the disturbance pressure eigenfunction:

$$D^2\hat{p} + \left\{\frac{2kD\bar{U}}{(\omega - k\bar{U})} - \frac{1}{\bar{\rho}}D\bar{\rho}\right\}D\hat{p} + \left\{\frac{\bar{\rho}\gamma_1 M_1^2}{\bar{\gamma}}(\omega - k\bar{U})^2 - k^2 - \beta^2\right\}\hat{p} = 0 \tag{2.9}$$

where

$$D = \frac{d}{dy}$$

$$\bar{\gamma} = \frac{c_{p_a}\bar{C}_a + c_{p_b}(1 - \bar{C}_a)}{c_{v_a}\bar{C}_a + c_{v_b}(1 - \bar{C}_a)}$$

and M_1 and γ_1 are, respectively, the Mach number and the ratio of specific heats of the high speed freestream.

The 2-D equation is obtained by setting $\beta = 0$ (3-D disturbances will be considered later).

$$D^2\hat{p} + \left\{\frac{2kD\bar{U}}{(\omega - k\bar{U})} - \frac{1}{\bar{\rho}}D\bar{\rho}\right\}D\hat{p} + \left\{\frac{\bar{\rho}\gamma_1 M_1^2}{\bar{\gamma}}(\omega - k\bar{U})^2 - k^2\right\}\hat{p} = 0 \qquad (2.10)$$

The above equation is solved subject to the boundary conditions

$$D\hat{p} = 0 \qquad y = \pm\frac{1}{2} \qquad (2.11)$$

which come from the y-momentum equation by setting the normal velocity at the wall to zero. The rest of the eigenfunctions can be found from the following equations:

$$\hat{v} = \frac{D\hat{p}}{i\bar{\rho}(\hat{\omega} - \hat{k}\bar{U})} \qquad (2.12a)$$

$$\hat{u} = \frac{i\hat{k}\hat{p} + \bar{\rho}D\bar{U}\hat{v}}{i\bar{\rho}(\hat{\omega} - \hat{k}\bar{U})} \qquad (2.12b)$$

$$\hat{\rho} = \frac{\bar{\rho}(i\hat{k}\hat{U} + D\hat{v}) + D\rho\hat{v}}{i(\hat{\omega} - \hat{k}\bar{U})} \qquad (2.12c)$$

$$\hat{c}_a = \frac{\hat{v} D \bar{C}_a}{i(\hat{\omega} - \hat{k}\bar{U})} \qquad (2.12d)$$

III. Basic Flow Profiles

Before the method by which the eigenvalues are obtained is discussed, it is necessary to discuss the basic velocity and density profiles used in this analysis. The choice of profiles has varied from using piecewise constant profiles to profiles obtained from numerical simulations. One of the simpler ways adopted by many researchers is to assume that the basic velocity has a form of a hyperbolic tangent profile. As stated in the Introduction Sandham and Reynolds[6] have shown that this is not a good approximation for the actual velocity profile obtained by solving the compressible boundary layer equations when there is high shear or a high density ratio. A better approximation is the use of a scaled variable based on Howarth's transformation for the variable in the hyperbolic tangent profile. Jackson and Grosch[14] demonstrated that this profile only gives qualitatively similar results when compared to the results obtained by using profiles found from the similarity solutions of the compressible boundary layer equations. Planché and Reynolds[32] showed that the profiles obtained by solving the O.D.E.'s obtained from the similarity transformation

of the compressible equations agreed very well with those found by numerical simulations. Because of the above reasons and reasons which will become evident later in this section, the profiles chosen for this analysis were obtained by solving the compressible boundary layer equations after making use of a similarity variable.

The boundary layer equations for a multi-species flow are given in Kuo[33]. For a two-species non-reacting system at constant pressure and $Pr = Sc = Le \cong 1$, they can be written as:

$$\frac{\partial}{\partial x^*}(\rho^* u^*) + \frac{\partial}{\partial y^*}(\rho^* v^*) = 0 \tag{3.1a}$$

$$\rho^* u^* \frac{\partial u^*}{\partial x^*} + \rho^* v^* \frac{\partial v^*}{\partial y^*} = \frac{\partial}{\partial y^*}\left(\mu^* \frac{\partial u^*}{\partial y^*}\right) \tag{3.1b}$$

$$\rho^* u^* \frac{\partial h_t^*}{\partial x^*} + \rho^* v^* \frac{\partial h_t^*}{\partial y^*} = \frac{\partial}{\partial y^*}\left(\mu^* \frac{\partial h_t^*}{\partial y^*}\right) \tag{3.1c}$$

$$\rho^* u^* \frac{\partial C_a}{\partial x^*} + \rho^* v^* \frac{\partial C_a}{\partial y^*} = \frac{\partial}{\partial y^*}\left(\mu^* \frac{\partial C_a}{\partial y^*}\right) \tag{3.1d}$$

$$p^* = \rho^* R^* T^* \tag{3.1e}$$

where $h_t^* = c_p^* T^* + \frac{u^{*2}}{2}$

The solution procedure used for these equations is almost identical to that used in Planché and Reynolds with one difference being that in our analysis the product of the viscosity, μ^*, and the density, ρ^*, is assumed to be constant ($\mu\rho = 1$) since the gas constant R is variable, instead of $\frac{\mu}{T} = 1$ as in their paper. Also, the transformation from the similarity variable, η, to the cross-stream coordinate, y, is done by integrating the following equation:

$$\frac{\partial y}{\partial \eta} = \frac{1}{\bar{\rho}}\sqrt{\frac{2x}{Re}} \qquad y(0) = 0$$

and the appropriate value of the quantity $\sqrt{\frac{2x}{Re}}$ is found from the condition $\delta_\omega = 1$.

Finally the profiles are re-non-dimensionalized using the height of the channel. In all cases considered the ratio of the vorticity thickness to the channel height is taken as $\frac{\delta_\omega^*}{H^*} = 0.1$ which corresponds to that used by Greenough *et al.*[16], Sigalla *et al.*[22,23] and Tam and Hu. This value of the vorticity thickness insures that the profiles have reached their freestream values far from the confining walls. It should be noted that the profiles used in this analysis are applicable for only small distances from the splitter plate.

As stated in the Introduction, the test case that is taken here is the one

used in Tam and Hu's analysis with the following properties:

$$M_1 = 4.5 \qquad M_2 = 1.6$$

$$\frac{a_1}{a_2} = 1.29 \qquad \gamma_1 = 1.67(He) \qquad \gamma_2 = 1.40(N_2)$$

Figure 2a,b and c show the profiles used in Tam and Hu's analysis and the ones calculated from the boundary layer equations. Besides the quantitative differences seen in the velocity and density profiles, a major qualitative difference is the existence of three extrema in the product of the basic density and the basic vorticity profiles $\bar{\rho}D\bar{U}$, as shown in Figure 2c. This phenomenon is dependent on the convective Mach number and the ratio of the specific heats. From Lees and Lin[34], it is known that the zeros of this product can give rise to neutral modes. In the unbounded case, Jackson and Grosch[4] showed that only one of these extrema is related to a critical neutral mode. This is the subsonic neutral mode whose eigenfunctions decay exponentially away from the mixing layer. However, for the bounded case, all three extrema can be associated with critical neutral modes, as we shall show.

It is also important to discuss the effect of the density ratio on the profiles which are calculated for our linear analysis. Figure 3 shows the velocity profiles

at a fixed convective Mach number and velocity ratio for different density ratios. It can be seen that as the density ratio is reduced from unity the high speed side has a "fuller" profile and the low speed side has a bigger defect. The opposite is true when the density ratio is increased from unity. Figure 4 shows the effect of the density ratio on $\bar{\rho}D\bar{U}$. It is evident that the emergence of the three extrema at a fixed convective Mach number and velocity ratio is dependent on the density ratio. For the parameters considered here the three extrema exist for approximately $1.1 < \rho_2 < 1.7$. The consequences of the multiple extrema will become evident in the later section where the characteristics of the instability modes are presented.

IV. Numerical Procedure For Finding The Eigenvalues

The numerical procedure used to find the eigenvalues is very similar to the method used in Tam and Hu. The method is a combination of the grid search method used for their vortex sheet problem and the numerical dispersion relation used for their finite shear problem and is described below.

Outside the shear layer ($|y| >> \frac{\theta^*}{H^*}$), $D\bar{u} \cong 0$. Therefore, equation (2.10) becomes the familiar vortex sheet equation with solutions:

$$\hat{p}(y) = A\,cos[\lambda_1(1-y)] \qquad \delta < y \leq 1 \tag{4.1a}$$

$$\hat{p}(y) = B\,cos[\lambda_2(1+y)] \qquad -\delta > y \geq -1 \tag{4.1b}$$

where

$$\lambda_1 = [M_1^2(\omega - kU_1)^2 - k^2]^{\frac{1}{2}} \tag{4.2a}$$

$$\lambda_2 = [M_1^2\left(\frac{a_1^*}{a_2^*}\right)^2(\omega - kU_2)^2 - k^2]^{\frac{1}{2}} \tag{4.2b}$$

Following Tam and Hu, equation (2.10) is integrated by a fourth order Runge-Kutta method from $-\delta$ (below the shear layer where equation (4.1b) holds) to $+\delta$ (above the shear layer where equation (4.1a) holds). The numerical solution at $y = \delta$, say $Bf(\delta)$, and its derivative are matched to the

corresponding solutions of equation (4.1a), thus giving rise to the following eigenvalue relation for $|\delta| >> \frac{\theta^*}{H^*}$.

$$W = -cos[\lambda_1(1-\delta)]f'(\delta) + \lambda_1 sin[\lambda_1(1-\delta)]f(\delta) = 0 \qquad (4.3)$$

The above equation is zero for specific values of (ω, k). There are two viewpoints taken when solving this eigenvalue problem, namely, the spatial and temporal viewpoints. In a temporal viewpoint, the wavenumber, k, is taken to be real and the frequency, ω, is the complex eigenvalue which is found by solving the above eigenvalue problem. Conversely, in a spatial viewpoint, the frequency is taken to be real and the wavenumber is the complex eigenvalue. The viewpoint chosen for a particular system usually depends on whether the instability is absolute or convective in nature; a temporal viewpoint is adopted for absolute instabilities, and a spatial viewpoint is chosen for convective instabilities arising due to an upstream wavemaker. Rigorous mathematical techniques exist based on the behavior of the impulse response of a system which dictate the appropriate viewpoint. For detailed discussions on this subject, the reader is referred to Briggs[35], Bers[36] and Huerre and Monkewitz[37]. For the current analysis a spatial viewpoint is adopted since both streams of the shear layer are supersonic and therefore all the eigenvalues are initially taken to be located in the upper-half of the complex wavenumber plane where

the frequency is complex and its imaginary part is a large positive number (Tam and Hu[15]).

To find the sets of values $(\omega_r, k_r + ik_i)$ for which equation (4.3) holds, a grid search procedure is employed. A coarse grid is used on the domain of interest in the complex k-plane. For a given ω, Im(W)=0 and Re(W)=0 are plotted by a contouring routine, and their intersection points are taken as the initial location of the roots. Then by the use of a Newton's iteration routine these eigenvalues are further refined. When performing this procedure, one must keep two things in mind. First, when ω and k are real, the integration contour for finding f(δ) must be deformed into the complex y-plane to avoid the critical layer. Thus the contour of integration must be deformed in such a way that it is below the critical layer singularity but above the singularities of the basic profiles in the complex y-plane. Second, one needs to distinguish between amplifying and evanescent waves. A good explanation for this procedure is given in Briggs and Tam and Hu. By following Briggs, if one needs to find the amplifying waves for a given real frequency Ω, then one first starts with a complex frequency $\Omega + i\Omega_I$, where Ω_I is a large enough positive number such that all the waves corresponding to the response of the system for $x < 0$ are in the lower half of the complex wave number plane and all the waves for $x > 0$ are in the upper half plane. Then the imaginary part of the frequency

is incremented to zero, while keeping the real part constant. The roots that drop below the real k-axis which were originally in the upper half plane are the amplifying waves for $x > 0$. Similarly, the roots starting from the lower half plane and crossing real k-axis represent amplifying waves for the $x < 0$ response.

V. Parameters and their Variation

In order to isolate the effect of basic flow density gradients from other effects such as shear and compressibility, the following method is proposed. The convective Mach number based on the current non-dimensionalization is given by:

$$M_c = \frac{U_1^* - U_2^*}{a_1^* + a_2^*} = \frac{M_1(1 - U_2)}{1 + \sqrt{\frac{\gamma_2}{\gamma_1 \rho_2}}} \tag{5.1}$$

In order to remove the first order compressibility effects, it is chosen to work with a constant convective Mach number. The above convective Mach number was shown by Papamoschou[31] to be a good parameter to describe the effects of compressibility. Also the velocity ratio $\frac{U_2^*}{U_1^*} = U_2$ is also taken to be constant. Jackson and Grosch[14] show that the maximum temporal growth

rate is proportional to $(1 - U_2)$. Although the consequences of varying this term for spatial calculations has not been investigated it was decided not to vary this term for our purposes. Another way to think about this condition comes from recognizing that if this term is unchanged then the difference in mean shear $(U_1^* - U_2^*)$ is unchanged. Therefore, as the density ratio $\frac{\rho_2^*}{\rho_1^*} = \rho_2$ is changed, the fast stream Mach number, M_1, is changed to keep the convective Mach number constant.

VI. Mode Labels

The convention used for the instability modes is the same as that used in Tam and Hu. All unstable modes whose phase velocity start from the velocity of the high speed stream will be labeled as Class A_{mn} modes and all unstable modes whose phase velocity start from the velocity of the low speed stream will be labeled as Class B_{mn} modes. The m and n subscripts are the 3-D and 2-D mode numbers respectively. The bulk of this paper will deal with the $m = 0$, i.e. a 2-D case.

VII. Results and Discussion

A. Test Case $\rho_2 = 1.398$

As stated earlier, the first case which is considered in this analysis is a test case based on the parameters used in the Tam and Hu analysis which correspond to $M_c = 1.836$, $\rho_2 = 1.398$, and $U_2 = 0.276$. For this case, the basic profiles have three generalized inflection points ($D(\bar{\rho}D\bar{U}) = 0$) which are summarized in Figure 5. Figure 6 shows the phase speed of the three different types of instability modes which are present for this case. The modes represented by the solid lines are the Class A modes which start from $C_{ph} = \frac{\omega}{k_r} = U_1$ which is a non-inflectional neutral solution. This type of solution is described in Mack[5,38] in conjunction with the boundary layer acoustic instabilities and is possible only when a trapped region of supersonic flow relative to the phase speed of the instability wave exists in the flow. Some of these modes, such as A_{01}, have wave velocities that are bounded by the velocity at the upper inflectional neutral point, and the others, such as A_{02}, remain unstable. The modes represented by the dashed lines are modes which start with a wave velocity equal to the mean velocity at the middle inflectional neutral point and which apparently have not been discussed so far in the literature. These modes will be labeled as Class C modes. Some of these modes have wave velocities which are bounded by the velocity at the upper inflectional neutral point and the other remain unstable. The third set of modes which are represented by the dash-dot lines are the Class B modes.

These modes start from $C_{ph} = U_2$ which is a non-inflectional neutral solution. The phase velocity of all of these modes are bounded by the velocity at the lower inflectional neutral point. It is clear that the use of a regular hyperbolic tangent profile based on the y coordinate would not give the results presented above (cf. Fig. 2c). Runs were made using a hyperbolic tangent profile, with the results being that both Class A and B modes terminated at the one and only inflection point. These results are shown in Figure 7.

Figure 8a,b and c show the spatial growth rates of the Class A, B and C modes respectively. The interesting thing to note here is that the C_{01} mode has the highest growth rate as opposed to the A_{01} mode when the hyperbolic tangent approximation is used. Furthermore, these modes are associated with a local minimum of $\bar{\rho}D\bar{U}$. In constant density or incompressible flows, instability is, of course, associated only with a maximum of vorticity.

The disturbance pressure eigenfunctions of the three modes at the maximum growth rates are given in Figures 9a,b and c. If one defines two convective Mach numbers M_{c1} and M_{c2} as:

$$M_{c1} = \frac{U_1^* - c_{ph}^*}{a_1^*} \tag{7.1a}$$

$$M_{c2} = \frac{c_{ph}^* - U_2^*}{a_2^*} \tag{7.1b}$$

where M_{c1} is the convective Mach number for stream 1 and M_{c2} is that for stream 2, then the modes with the maximum growth rates in each Class, i.e. A_{03}, B_{04} and C_{01}, can be described in the following manner. The A_{03} mode is supersonic with respect to the slower stream and subsonic with respect to the high speed stream. This can be seen in the shape of the eigenfunction which is monotone in the upper half of the channel and oscillatory in the lower half. The opposite is true for the B_{04} mode. The C_{01} mode is supersonic with respect to both streams and shows an oscillatory behavior over the entire channel height.

Another difference observed when using the profiles based on the compressible boundary layer equations as opposed to the hyperbolic tangent profiles is the magnitude of the eigenfunctions. When the hyperbolic tangent profiles are used the eigenfunction with the maximum magnitude is the streamwise perturbation velocity eigenfunction. This is not true for the boundary layer profiles where the perturbation density eigenfunction possesses the largest magnitude.

B. Increasing Density Ratio

Next, the density ratio is increased to $\rho_2 = 3.0$. Different results were obtained for this case ranging from the change in basic profiles to the growth rates and eigenfunction magnitudes. First, the results for this density ratio

will be given and then the changes that occur between $1.398 < \rho_2 < 3.0$ will be discussed by considering some intermediate cases.

The basic profiles have only one generalized inflection point for $\rho_2 = 3.0$. The velocity at that point is close to that of the low speed stream. This is illustrated in Figure 10. Figure 11 shows the phase speed of the instability waves present in this case. The Class A modes show similar behavior to the ones present in the case of $\rho_2 = 1.398$; however there are more Class A modes present in the same frequency range considered. Also, since two of the inflectional neutral points are not present, these modes now remain unstable. The Class B modes, however, are very different. In this frequency range only the B_{01} mode has a growth rate which is higher than 0.01. The phase speeds of the rest of the Class B modes (not shown) start at the velocity at the non-inflectional neutral point $C_{ph} = U_2$ and end at the velocity at the inflectional neutral point. These modes have very small growth rates. It will be shown later that, due to several factors as the density ratio is increased, a linear resonance occurs between the Class B modes which results in the particular configuration of the Class B modes shown in the figure. The growth rate of the Class A modes and the B_{01} modes are given in Figures 12a and b. The many peaks present in the growth rate curve of the B_{01} mode is characteristic of the linear resonance (see below) which is occurring. It is interesting to note that

the peaks located at $\omega = 5.775$ and $\omega = 6.62$ have growth rates $-k_i = 0.7401$ and 0.7404 respectively. These two are almost identical and so both frequencies might be excited in the nonlinear portion of shear layer evolution. Also, this mode possesses the highest growth rate among all the modes and has twice the growth rate of the maximum growth rate for the $\rho_2 = 1.398$ case. This trend continues at higher density ratios and will be discussed further when the results for the case of $\rho_2 = 7.0$ are presented.

Figure 13 shows the phase speed of the B_{01} mode only. It can be seen that the phase speed has an oscillatory behavior and becomes neutral after many oscillations. This behavior can also be attributed to the linear resonance and will also be discussed later. Another interesting result is observed in the behavior of the eigenfunctions. The eigenfunctions for the density and species concentration show large spikes near the critical layer and the magnitude of the density eigenfunction is two orders of magnitude higher than the velocity and pressure eigenfunctions. Figure 14a,b,c,d and e show the eigenfunction for the B_{01} mode at the first growth rate peak ($\omega = 5.775$) . The eigenfunctions at the second peak are very similar to those of the first peak. For comparison, Figure 14c also shows the perturbation density eigenfunction at the maximum growth of the test case which is normalized with respect to the eigenfunction magnitudes of the test case.

The next step will be to show the emergence of the different phenomena described above by analyzing the instability characteristics for density ratios between 1.398 and 3.0. As the density ratio is increased from 1.398, the upper and middle inflection points begin to move towards one another and the lower inflection point moves lower such that the velocity at that inflection point tends towards U_2. At $\rho_2 \approx 1.71$ the upper and middle inflection points coalesce, and beyond that density ratio they disappear. This movement of the inflection points, i.e. changes in the basic profiles due to the effects of the density ratio, lead to a linear resonance between the Class B modes, as discussed below.

In order to show that the interaction between the modes is indeed a resonant interaction, a series of figures are provided showing how the modes coalesce and interact. First, Figure 15 shows the phase speed of the Class B modes for $\rho_2 = 1.398$ and $\rho_2 = 1.8$. As the density ratio is increased in this range the lower inflectional neutral phase speed decreased from 0.4 to 0.37. As this happens the curved parts of the phase speed curvse of the B_{01} mode and the B_{02} mode connect at a density ratio between 1.398 and 1.8. As the density ratio is increased beyond that point, calculations show that the neutral phase speed decreases and the curves separate leaving the B_{01} with the upper curved portion of the old B_{02}. This process continues and for $\rho_2 = 1.8$, as the figure shows, five of the original Class B modes have interacted. This type of process

is well described in Craik(1985). Figure 16 shows the growth rate curves for the two density ratios, and again it is possible to see the how the curve for $\rho_2 = 1.8$ evolves from the others. We should also note that for $\rho_2 = 1.8$ the growth rates of the $B_{02} - B_{05}$ modes are not shown because the magnitude of the growth rates is less than 0.01. Finally, Figure 17a and b show the phase speed and growth rates of the Class B modes for only $\rho_2 = 1.8$. On these figures the location where the higher modes become neutral are shown with the vertical dotted lines. The purpose of these figures is to show that these neutral frequencies correspond well with frequencies corresponding to the local minima of the B_{01} mode, cf. Fig. 16.

Figure 18 shows the growth rate of the B_{01} for different density ratios. It is clear from this figure that as the density ratio is increased more and more Class B modes have resonant interactions with one another to cause the B_{01} mode to have more and more peaks. Figure 19 shows the number of peaks in the growth rate curves as a function of the density ratio. It is clear that this is a non-linear step function of the density.

Also, as the density ratio is increased, the phase speed of the B_{01} mode, which is the mode with the maximum growth rate, becomes more and more asymmetric. This type of phenomenon is observed in the experiments conducted by Papamoschou[31]. In his experiments, he observed that: "in su-

personic combinations M_{c1} is always highest ($U_c \rightarrow U_2$) while in supersonic-subsonic combinations, M_{c2} is always highest ($U_c \rightarrow U_1$)". In our analysis, an increase of the density ratio from the test case increased M_2 and lowered M_1 causing both Mach numbers to be between 2 and 4. Decreasing the density ratio increased M_1 and decreased M_2 such that M_2 became almost sonic.

The final comment which needs to be made concerns the effect of the density ratio on the growth rate of the modes. After all, this is one of the limiting factors in the design of supersonic combustors. Figure 20 shows the growth rate of the B_{01} mode for $\rho_2 = 7.0$. This growth rate is nearly 400% greater than the growth rate at $\rho_2 = 1.398$. This type of increase in the growth rate as a function of the density ratio is supported by observations made by Brown and Roshko[28] who stated that growth rates in supersonic shear layers are more sensitive to changes in the density ratio than subsonic shear layers and that increases of up to 300% in growth rates were observed in supersonic shear layers.

Figure 21 shows the maximum growth rate as a function of density ratio for the cases where mode B_{01} has become dominant. Density ratios from 2.0 to 13 have been considered. Some leveling off of the curve is noticed as the density ratio is increased.

The effect of the density ratio on the Class A modes varies from mode to

mode. For density ratios where Class C modes still exist, increasing the density ratio slightly increases or decreases the growth rate of some Class C modes and some Class A modes. These modes eventually coalesce and interact, and once the upper two inflection points disappear, only the Class A modes remain. As the density ratio is increased from 3.0 to 7.0 so that no Class C modes exist, the most unstable mode, A_{01}, practically has a nearly constant growth rate, and the other Class A modes actually have lower growth rates.

C. Decreasing the Density Ratio

When the density ratio is decreased from the test case, almost the opposite of the previous case occurs. First, the lower and middle inflection points move towards one-another and eventually coalesce and disappear. The upper inflection point remains and tends upwards so that the inflectional neutral velocity tends towards U_1. These two effects should lead to a resonant interaction between the Class A modes.

To investigate the above conjecture, two density ratios were considered, $\rho_2 = \frac{1}{3}$ and $\rho_2 = \frac{1}{7}$. In order to keep the convective Mach number constant, the gases in the mixing layer were changed to Ar in the fast stream and CH_4 in the slow stream. This was done so that the Mach number of the slow stream remained supersonic ($M_2 = 1.159$ for $\rho_2 = \frac{1}{3}$ and $M_2 = 1.000$ for $\rho_2 = \frac{1}{7}$).

Figure 22 shows the phase speed of the Class A and B modes for $\rho_2 = \frac{1}{3}$. The Class B modes (B_{02} and on) remain unstable, and within the same frequency range ($0 < \omega < 5$) there are more Class B modes than in the $\rho_2 = 1.398$ case. A difference arises in the behavior of the B_{01} mode. For this density ratio, this mode becomes neutral at the upper inflectional neutral point. Recall that for $\rho_2 = 3.0$, the A_{01} mode did not have the corresponding behavior. Now, the A_{01} mode for this case interacts with the modes $A_{03} - A_{05}$. However, the A_{02} mode is not involved in this interaction and remains unstable. Figures 23a and b show the growth rates for the Class A and B Modes. It is clear that both the A_{01} and A_{02} modes have appreciable growth rates, and again like the higher Class B modes in the case of $\rho_2 = 3.0$, the higher Class A modes ($A_{03} - A_{05}$) have growth rates which are less than 0.01. Due to the linear resonance occurring between some of the modes, the growth rate of the A_{01} mode (the maximum growth rate for this density ratio) is greater than the maximum growth rate for the $\rho_2 = 1.398$ case. However, the maximum growth rate for this case is only slightly higher than the test case. The growth rate of the Class B modes are smaller for this density ratio as compared to the test case.

When the density ratio is decreased to $\rho_2 = \frac{1}{7}$, more interactions occur between the modes which is a bit more interesting. Figure 24 shows the phase

speed of the modes present at this density ratio. Comparing this figure to Figure 22, one can see several changes. As the density ratio is decreased from $\frac{1}{3}$ to $\frac{1}{7}$, modes B_{01}, A_{01} and A_{02} interact with one another which causes the B_{01} mode to be the dominant mode. Looking closely at the two figures the transition between them can be realized. First, just as there are more and more Class B modes in a certain frequency range as the density ratio decreases, there are fewer and fewer Class A modes. As the density ratio is decreased the B_{01} mode in Figure 22 interacts with the A_{02} mode near the inflectional neutral point. Then this new B_{01} mode, which has picked up the majority of the A_{02} mode's curve, interacts with the A_{01} mode. This final interaction causes the B_{01} mode to be the mode which exhibits a linear resonance with the rest of the Class A modes. Actually at this density ratio more than 25 Class A modes are involved in this resonant interaction. Figure 25 shows the growth rate for the B_{01} mode. Notice the unstable bandwidth which is many factors above any other mode considered at any density ratio. However, the increase in growth rate from the $\rho_2 = \frac{1}{3}$ case is only about 0.05.

VIII. Concluding Remarks

The effects of density gradients on the linear stability characteristics of the acoustic wall modes in a confined supersonic shear layer were studied. A

test case based on the analysis of Tam and Hu[15] was chosen. A new class of modes was discovered for this case which was due to the emergence of three generalized inflection points in the $\bar{\rho}D\bar{U}$ profile. This new mode has the highest growth rate for the test case density ratio and is associated with the local minima of the $\bar{\rho}D\bar{U}$ profile.

Next, the case of increasing density ratio was considered. Increasing the density ratio caused the $\bar{\rho}D\bar{U}$ profile to eventually have only one inflection point, with a velocity close to that of the low speed stream. This in turn led to a linear resonance between the Class B modes. As the density ratio was increased, more and more Class B modes were involved in the resonant interaction. Another phenomenon observed for this case was the increase in the growth rate as the density ratio increased. This increase in the growth rate seems to continue as the density ratio is increased with only some leveling of the curve noticed at the highest density ratio. Two effects can contribute to this increase. The first is the shape of the velocity profile. As the density ratio is increased the velocity is "fuller" on the low speed side which in turn results in higher growth rates as observed by Sandham and Reynolds[6] in relation to the subsonic shear layer. The second effect has to due with the linear interaction of the modes which causes the "strengthening" of the first mode.

As the density ratio was decreased, the $\bar{\rho}D\bar{U}$ profile also lost two out of

the three inflection points. However, the remaining inflection point was the opposite of the one for the increasing density ratio case, with the velocity at the remaining inflection point being close to that of the high speed stream. This led to an interaction between the Class A modes, and for very low density ratios, also the B_{01} mode. The increases in the growth rates for this case are small compared to the increasing density ratio. This is due to the fact that as the density ratio is decreased the velocity profile is "fuller" on the high speed side which tends to reduce the growth rate. This nearly offsets the effect of the linear resonance.

A major conclusion which can be drawn from this analysis is that when a much heavier gas occupies the slow stream of a supersonic confined mixing layer, the growth rate can be increased by 4-5 factors from the case when the densities of the two gases are nearly equal. These high growth rates are comparable to the incompressible growth rates and could lead to better mixing in different applications.

ACKNOWLEDGMENTS

This work was supported by NASA Grant NCC2-374.

References

[1]Blumen, W. "Shear layer instability of an inviscid compressible fluid", **J. Fluid Mech., 40**, 769-781, (1970).

[2] Blumen, W., Drazin, P.G. and Billings, D.F. "Shear layer instability of an inviscid compressible fluid. Part 2", **J. Fluid Mech., 71**, 305-316, (1975).

[3]Drazin, P.G. and Garvey, A. "Shear layer instability of an inviscid compressible fluid. Part 3", **J. Fluid Mech. 82**, 255-260, (1977).

[4]Jackson, T.L. and Grosch, C.E. (1989) "Inviscid spatial stability of a compressible mixing layer", **J. Fluid Mech., 208**, 609-637, (1989).

[5]Mack, L. M., "On the inviscid acoustic-mode instability of supersonic shear flows–Part 1: Two-Dimensional waves", **Theoret. Comput. Fluid Dynamics, 2**, 97-123, (1990).

[6]Sandham, N.D. and Reynolds, W.C., "A numerical investigation of the compressible mixing layer", Report No. TF-45. Thermosciences Division, Mechanical Engineering Department, Stanford University, (1989).

[7]Sandham N.D. and Reynolds, W.C. "Three-Dimensional simulations of large eddies in the compressible mixing layer", **J. Fluid Mech., 224**, 133-158, (1991).

[8]Gropengiesser, H. "Study on the stability of boundary layers and compressible fluids", NASA TT F12786, (1970).

[9]Lessen, M., Fox, J.A. and Zien, H.M. "On the inviscid stability of the laminar mixing of two parallel streams of a compressible fluid", **J. Fluid Mech., 23**, 355-367, (1965).

[10]Lessen, M., Fox, J.A. and Zien, H.M. "Stability of the laminar mixing of two parallel streams with respect to supersonic disturbances", **J. Fluid Mech., 25**, 737-742, (1966).

[11]Ragab, S.A. and Wu, J.L. "Linear instabilities in two- dimensional Compressible mixing layers", **Phys. Fluids A, 1**, 957-966, (1989).

[12]Ragab, S.A. and Wu, J.L. "Linear subharmonic instabilities of periodic compressible mixing layers", **AIAA Paper No. 89-0039**, (1989).

[13]Ragab, S.A. and Wu, J.L. "Instabilities of supersonic shear flow", **AIAA Paper No. 90-0712**, (1990).

[14]Jackson, T.L. and Grosch, C.E. "Inviscid spatial stability of a compressible mixing layer. Part 3. Effect of thermodynamics", **J. Fluid Mech., 224**, 159-175, (1991).

[15]Tam, C.K.W. and Hu, F.Q. "The instability and acoustic wave modes of supersonic mixing layers inside a rectangular channel", **J. Fluid Mech., 203**, 51-76, (1989).

[16]Greenough, J., Riley, J., Soetrisno, M. and Eberhardt, D. "The effect of walls on a compressible mixing layer", **AIAA Paper No. 89-0372**, (1989).

[17]Hu, F.Q. Private Communication (1994).

[18]Zhuang, M., Dimotakis, P.E., and Kubota, T., "The effect of walls on a spatially growing supersonic shear layer", **Phys. Fluids A, 2** 599-604, (1990).

[19]Morris, P.J., and Giridharan, M.G., "The effect of walls on the instability waves in supersonic shear layers", **Phys. Fluids A, 3** 356-358, (1991).

[20]Lele, S.K. "Direct numerical simulation of compressible free shear flows", **AIAA Paper No. 89-0374**, (1989).

[21]Ragab, S.A. and Sheen, S., "Numerical simulation of a compressible mixing layer", **AIAA Paper No. 90-1669**, (1990).

[22]Sigalla, L., Eberhardt, D., Greenough, J., Riley, J. and Soetrisno, M. "Numerical simulation of confined, spatially-developing mixing layers: comparison to the temporal shear layer", **AIAA Paper No. 90-1462**, (1990).

[23]Sigalla, L., Eberhardt, D., Greenough J. and Riley, J. "Numerical simulation of confined, spatially developing shear layers: Nonlinear interaction between instability modes", **AIAA Paper No. 91-1643**, (1991).

[24]Huang, H.-S. and Riley, J.J. "Transition to turbulence in confined, compressible mixing layers. Part I: 3-D numerical simulations with excitation of random, broadband white noise", **AIAA Paper No. 92-05532**, (1992).

[25]Lu, P.J. and Wu, K.C. "On the shock enhancement of confined supersonic mixing layers", **Phys. Fluids A, 3**, 3046-3062, (1991a).

[26]Lu, P.J. and Wu, K.C. "Numerical investigation on the structure of a confined supersonic mixing layer", **Phys. Fluids A, 3**, 3063-3079, (1991b).

[27]Gathmann, R.J., Si-Ameur, M. and Mathey, F. "Numerical simulations of three-dimensional natural transition in the compressible confined shear layer", **Phys. Fluids A, 5**, 2946-2968, (1993).

[28]Brown, G.L. and Roshko, A. "On density effects and large structure in turbulent mixing layers", **J. Fluid Mech., 64**, 775-816, (1974).

[29]Papamoschou, D. and Roshko, A. "Observations of supersonic free shear layer", **AIAA Paper No. 86-0126**, (1986).

[30]Papamoschou, D. and Roshko, A. "The compressible turbulent shear layer; an experimental study", **J. Fluid Mech., 197**, 453-477), (1988).

[31]Papamoschou, D. "A structure of the compressible turbulent shear layer", **AIAA Paper No. 89-0126**, (1989).

[32]Planche, O.H. and Reynolds, W.C. "A Numerical investigation of the compressible reacting mixing layer", Report No. TF-56. Thermosciences Division, Mechanical Engineering Department, Stanford University, (1992).

[33]Kuo, K.K., Principles of Combustion, Wiley Interscience (1982).

[34]Lees, L., and Lin, C.C., "Investigation of the stability of the laminar boundary layer in a compressible fluid", **NACA Technical Note No. 1115**, (1946).

[35]Briggs, R.J. **Electron-Stream interaction with plasmas**, Research Monograph No. 29. Cambridge, Mass: M.I.T. Press, (1964).

[36]Bers, A. "Linear waves and instabilities", **In Physique des Plasmas** (ed. C. DeWitt & J. Peyraud), pp. 117-213, (1975). New York: Gordon and Breach.

[37]Huerre, P. and Monkewitz, P.A. (1990) "Local and global instabilities in spatially developing flows", **Annu. Rev. Fluid Mech., 22**, 473-537, (1990).

[38]Mack, L.M., "Boundary-Layer stability theory". In *Special Course on Stability and Transition of Laminar Flow*, **AGARD Report No. 709**, 3-1 to 3-81, (1984).

List of Figures

Figrue 1. Model used for the analysis of the compressible shear layer.

Figure 2a. Base velocity profiles for the test case.

Figure 2b. Base density profiles for the test case.

Figure 2c. Base density times base vorticity ($\bar{\rho}D\bar{U}$) profiles for the test case.

Figure 3. Base velocity profiles calculated from the boundary layer equations for different density ratios at a fixed convective Mach number ($M_c = 1.836$) and velocity ratio ($U_2 = 0.276$).

Figure 4. Base density times base vorticity ($\bar{\rho}D\bar{U}$) calculated from the boundary layer equations for different density ratios at a fixed convective Mach number ($M_c = 1.836$) and velocity ratio ($U_2 = 0.276$).

Figure 5. Graph of $D(\bar{\rho}D\bar{U})$ for the test case. Zeros are given by the vertical dotted lines. (Boundary layer profiles)

Figure 6. Phase speed vs. frequency for the unstable modes present in the flow at the test case parameters.

Figrue 7. Phase speed vs. frequency for the unstable modes present in the flow at the test case parameters. (Hyperbolic Tangent profiles)

Figure 8a. Spatial growth rate vs. frequency for the Class A modes at the test case parameters.

Figure 8b. Spatial growth rate vs. frequency for the Class B modes at the test case parameters.

Figure 8c. Spatial growth rate vs. frequency for the Class C modes at the test case parameters.

Figure 9a. Disturbance pressure eigenfunction for the A_{03} mode at the maximum growth rate. (Test case parameters)

Figure 9b. Disturbance pressure eigenfunction for the B_{04} mode at the maximum growth rate. (Test case parameters)

Figure 9c. Disturbance pressure eigenfunction for the C_{01} mode at the maximum growth rate. (Test case parameters)

Figure 10. Graph of $D(\bar{\rho}D\bar{U})$ for $\rho_2 = 3.0$. Only one zero exists and is given by the vertical dotted line.

Figure 11. Phase speed vs. frequency for the unstable modes present in the flow at $\rho_2 = 3.0$. Higher Class B modes (B_{02} and on) not shown.

Figure 12a. Spatial growth rate vs. frequency for the Class A modes at $\rho_2 = 3.0$.

Figure 12b. Spatial growth rate vs. frequency for the B_{01} mode at $\rho_2 = 3.0$.

Figure 13. Phase speed vs. frequency for the B_{01} mode at $\rho_2 = 3.0$.

Figure 14a. Streamwise disturbance velocity eigenfunction for the B_{01} mode for $\rho_2 = 3.0$ and at the first maximum growth rate peak $\omega = 5.775$).

Figure 14b. Cross-stream disturbance velocity eigenfunction for the B_{01} mode for $\rho_2 = 3.0$ and at the first maximum growth rate peak $\omega = 5.775$).

Figure 14c. Disturbance density eigenfunction for the B_{01} mode for $\rho_2 = 3.0$ and at the first maximum growth rate peak $\omega = 5.775$), and for the C_{01} for $\rho_2 = 1.398$ at $\omega = 1.75$).

Figure 14d. Disturbance pressure eigenfunction for the B_{01} mode for $\rho_2 = 3.0$ and at the first maximum growth rate peak $\omega = 5.775$).

Figure 14e. Disturbance species concentration eigenfunction for the B_{01} mode for $\rho_2 = 3.0$ and at the first maximum growth rate peak $\omega = 5.775$).

Figure 15. Phase speed vs. frequency for the Class B modes at density ratios of 1.398 and 1.8.

Figure 16. Spatial growth rate vs. frequency for the Class B modes at $\rho_2 = 1.398$ and the B_{01} mode at $\rho_2 = 1.8$.

Figure 17a. Phase speed vs. frequency for the Class B modes at $\rho_2 = 1.8$. Vertical dotted lines represent locations where the higher modes become neutral.

Figure 17b. Spatial growth rate vs. frequency for the B_{01} mode at $\rho_2 = 1.8$. Vertical dotted lines represent locations where the higher modes become neutral.

Figure 18. Spatial growth rate vs. frequency for the B_{01} mode at different density ratios.

Figure 19. Growth rate peaks (number of oscillations) vs. density ratio for the B_{01} mode.

Figure 20. Spatial growth rate vs. frequency for the B_{01} mode at $\rho_2 = 7.0$.

Figure 21. Maximum spatial growth rate vs. density ratio for the B_{01} mode.

Figure 22. Phase speed vs. frequency for the unstable modes present in the flow at $\rho_2 = \frac{1}{3}$.

Figure 23a. Spatial Growth rate vs. frequency for the Class A modes at $\rho_2 = \frac{1}{3}$.

Figure 23b. Spatial Growth rate vs. frequency for the Class B modes at $\rho_2 = \frac{1}{3}$.

Figure 24. Phase speed vs. frequency for the unstable modes present in the flow at $\rho_2 = \frac{1}{7}$.

Figure 25. Spatial Growth rate vs. frequency for the B_{01} mode at $\rho_2 = \frac{1}{7}$.

Figure 1

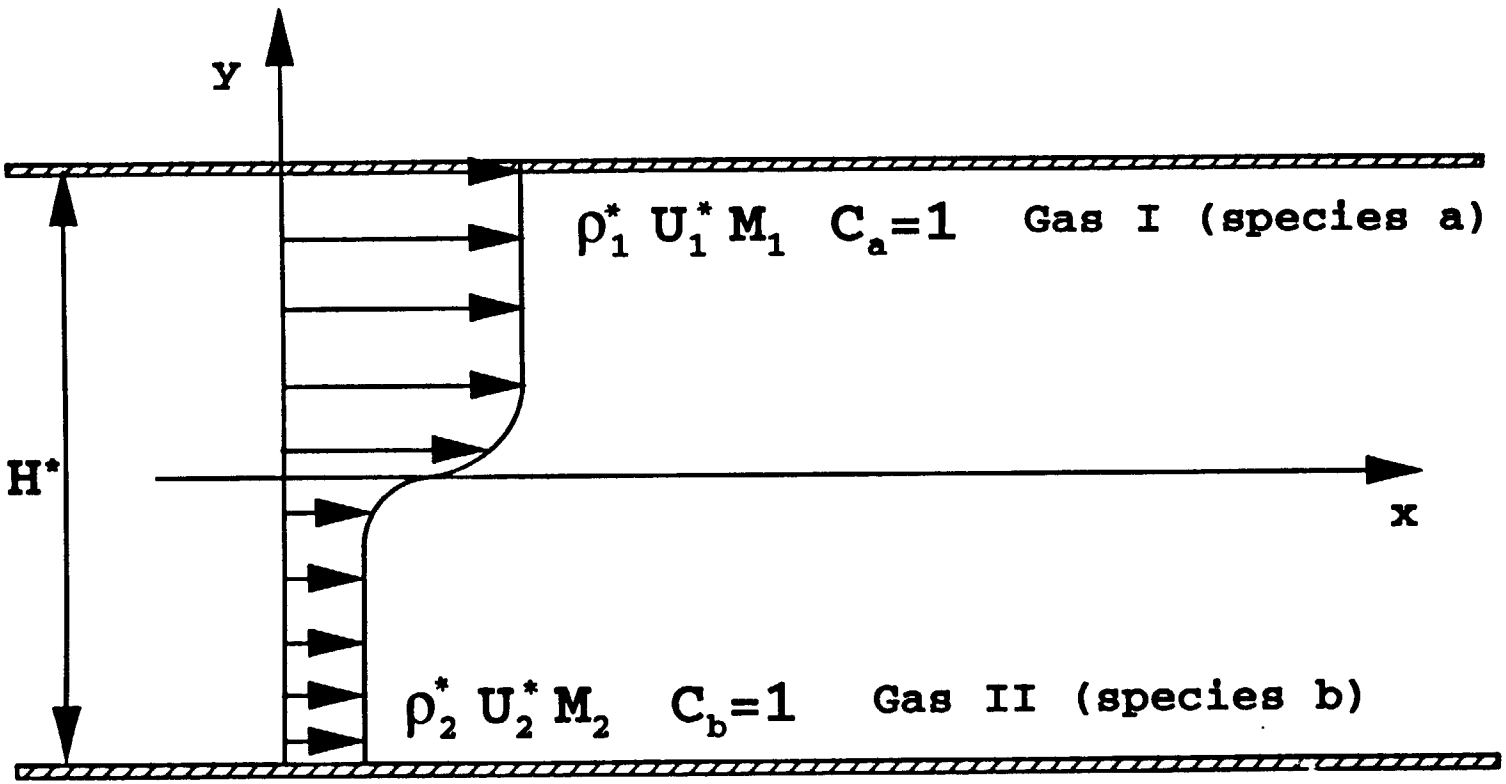
y
$\rho_1^* U_1^* M_1$ $C_a=1$ Gas I (species a)
H^*
x
$\rho_2^* U_2^* M_2$ $C_b=1$ Gas II (species b)

Figure 2a

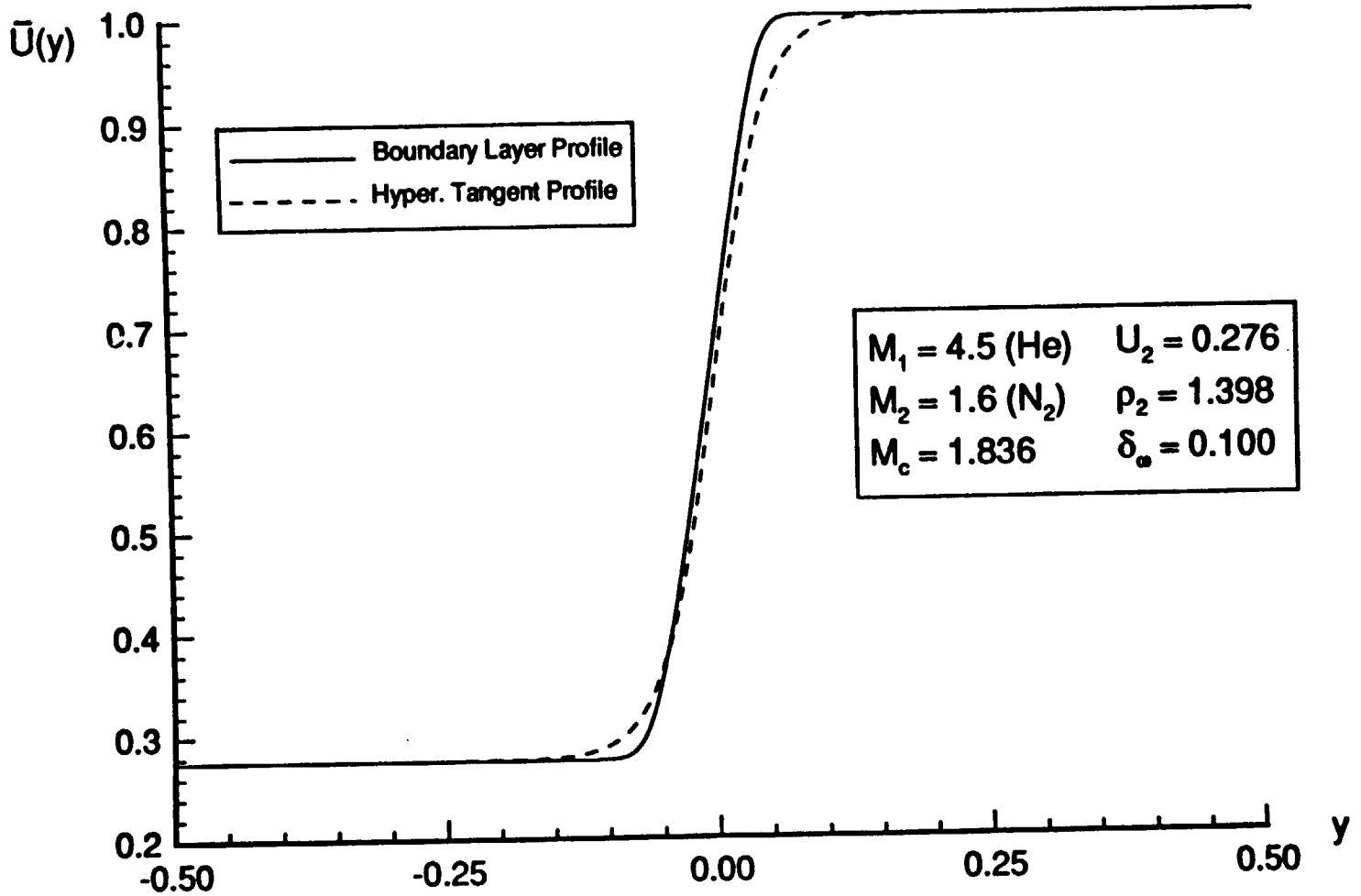
Ū(y)
1.0
0.9
0.8
0.7
0.6
0.5
0.4
0.3
0.2
-0.50
-0.25
0.00
0.25
0.50
y
Boundary Layer Profile
Hyper. Tangent Profile
M1 = 4.5 (He)
M2 = 1.6 (N2)
Mc = 1.836
U2 = 0.276
ρ2 = 1.398
δω = 0.100

Figure 2b

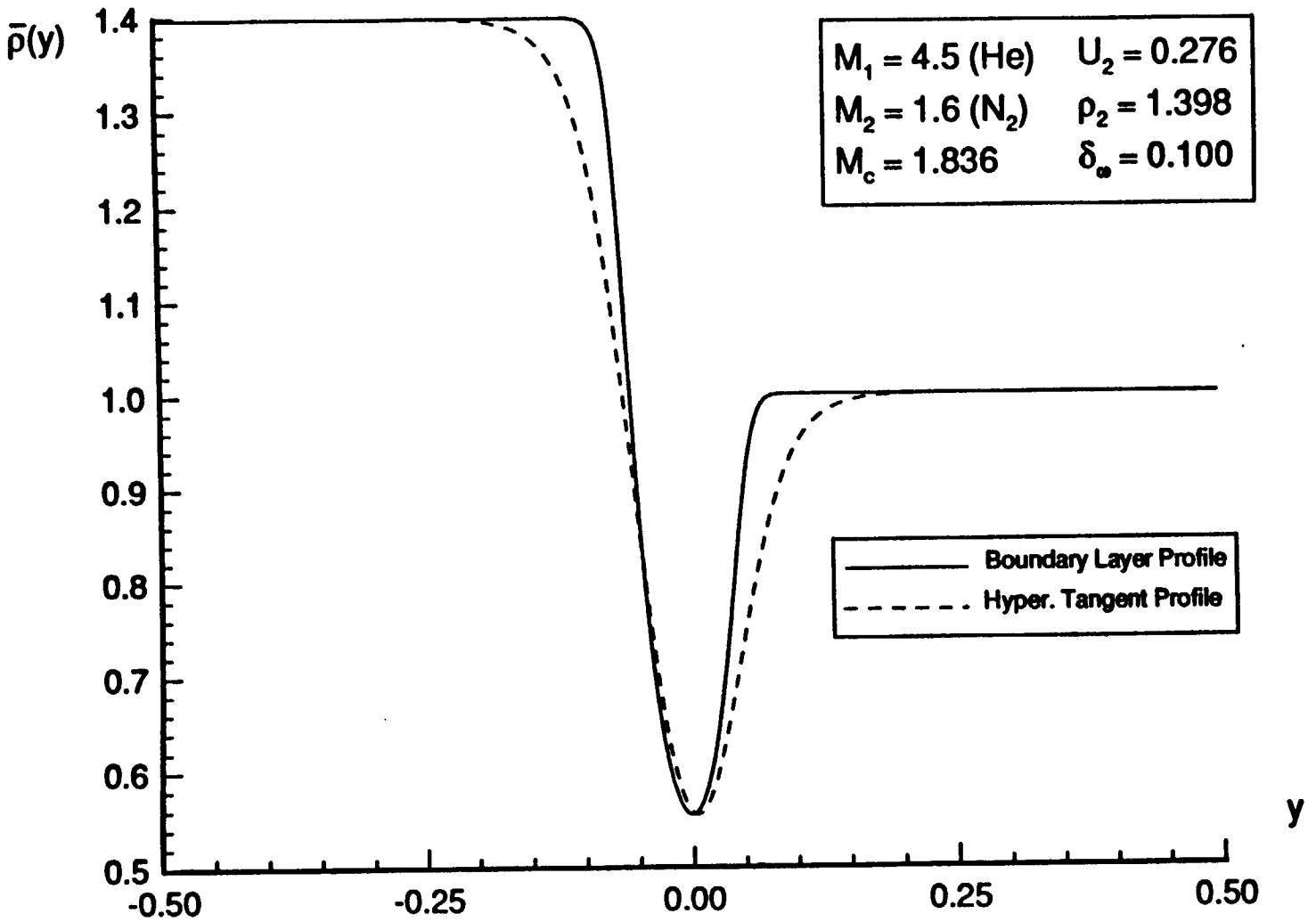
$\bar{\rho}(y)$
1.4
1.3
1.2
1.1
1.0
0.9
0.8
0.7
0.6
0.5
-0.50
-0.25
0.00
0.25
0.50
y
$M_1 = 4.5$ (He)
$U_2 = 0.276$
$M_2 = 1.6$ (N_2)
$\rho_2 = 1.398$
$M_c = 1.836$
$\delta_\infty = 0.100$
Boundary Layer Profile
Hyper. Tangent Profile

Figure 2c

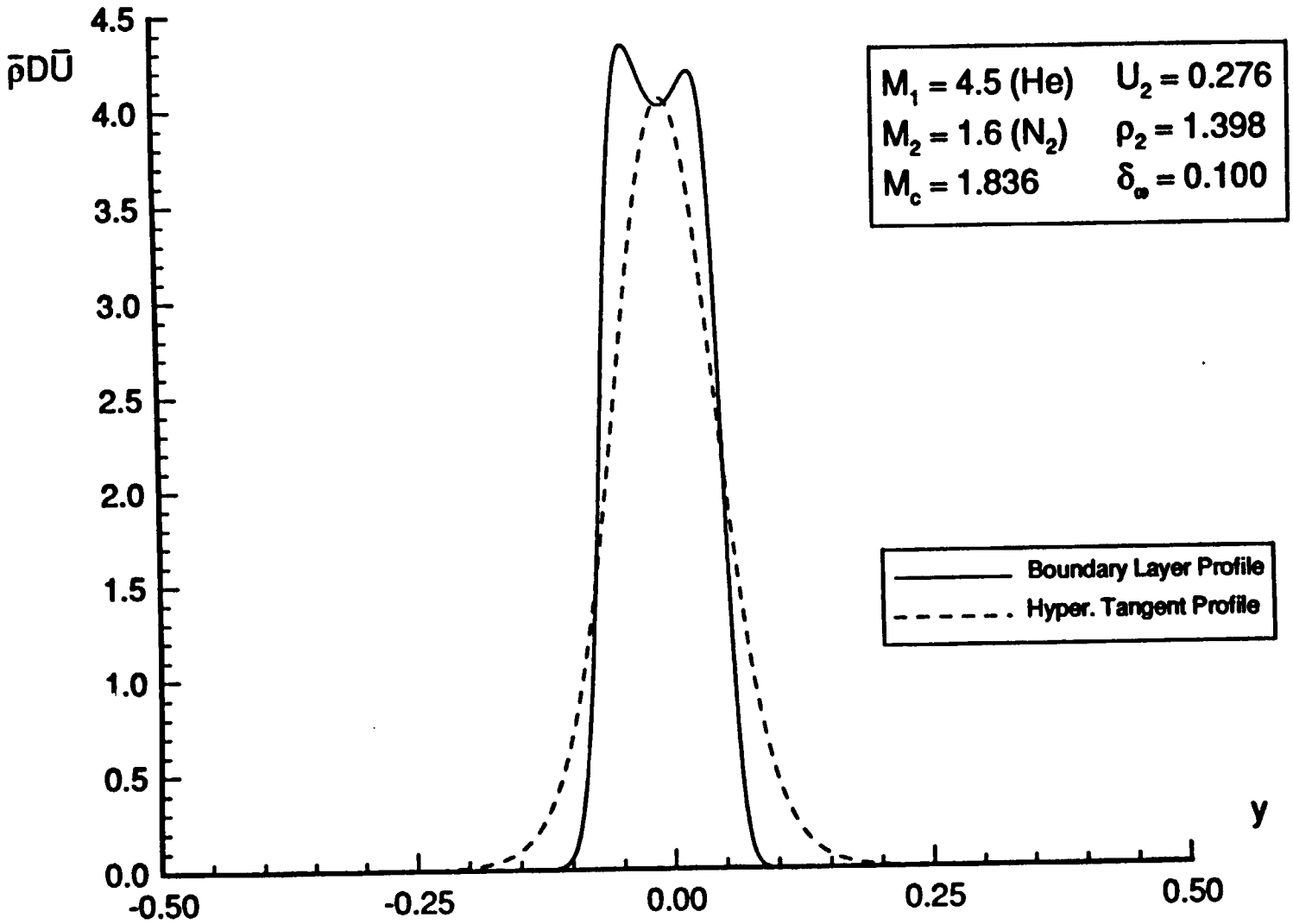
$\tilde{\rho}D\bar{U}$
4.5
4.0
3.5
3.0
2.5
2.0
1.5
1.0
0.5
0.0
-0.50
-0.25
0.00
0.25
0.50
y
$M_1 = 4.5$ (He)
$U_2 = 0.276$
$M_2 = 1.6$ (N_2)
$\rho_2 = 1.398$
$M_c = 1.836$
$\delta_\omega = 0.100$
Boundary Layer Profile
Hyper. Tangent Profile

Figure 3

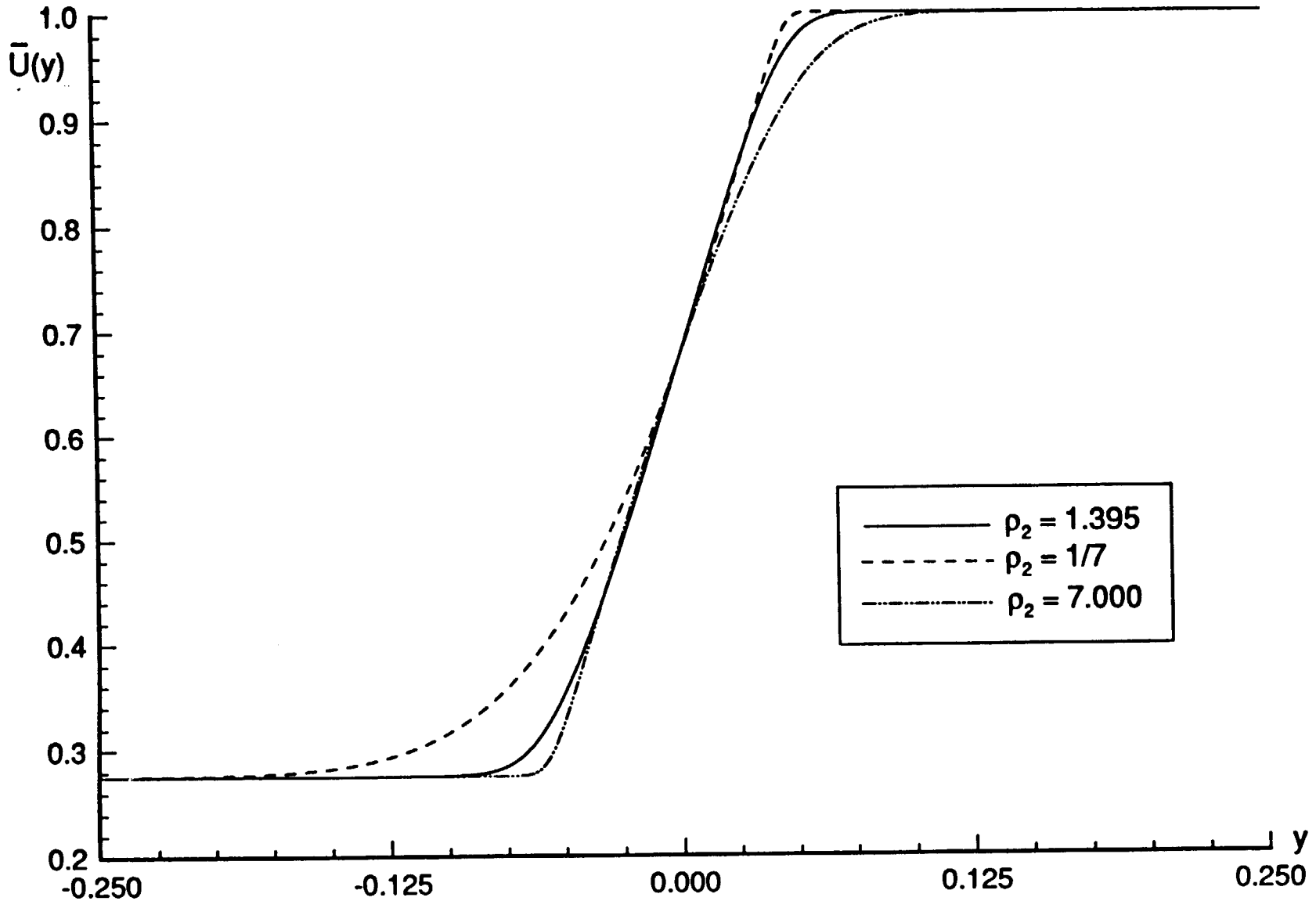
1.0
$\bar{U}(y)$
0.9
0.8
0.7
0.6
0.5
0.4
0.3
0.2
-0.250
-0.125
0.000
0.125
0.250
y
$\rho_2 = 1.395$
$\rho_2 = 1/7$
$\rho_2 = 7.000$

Figure 4

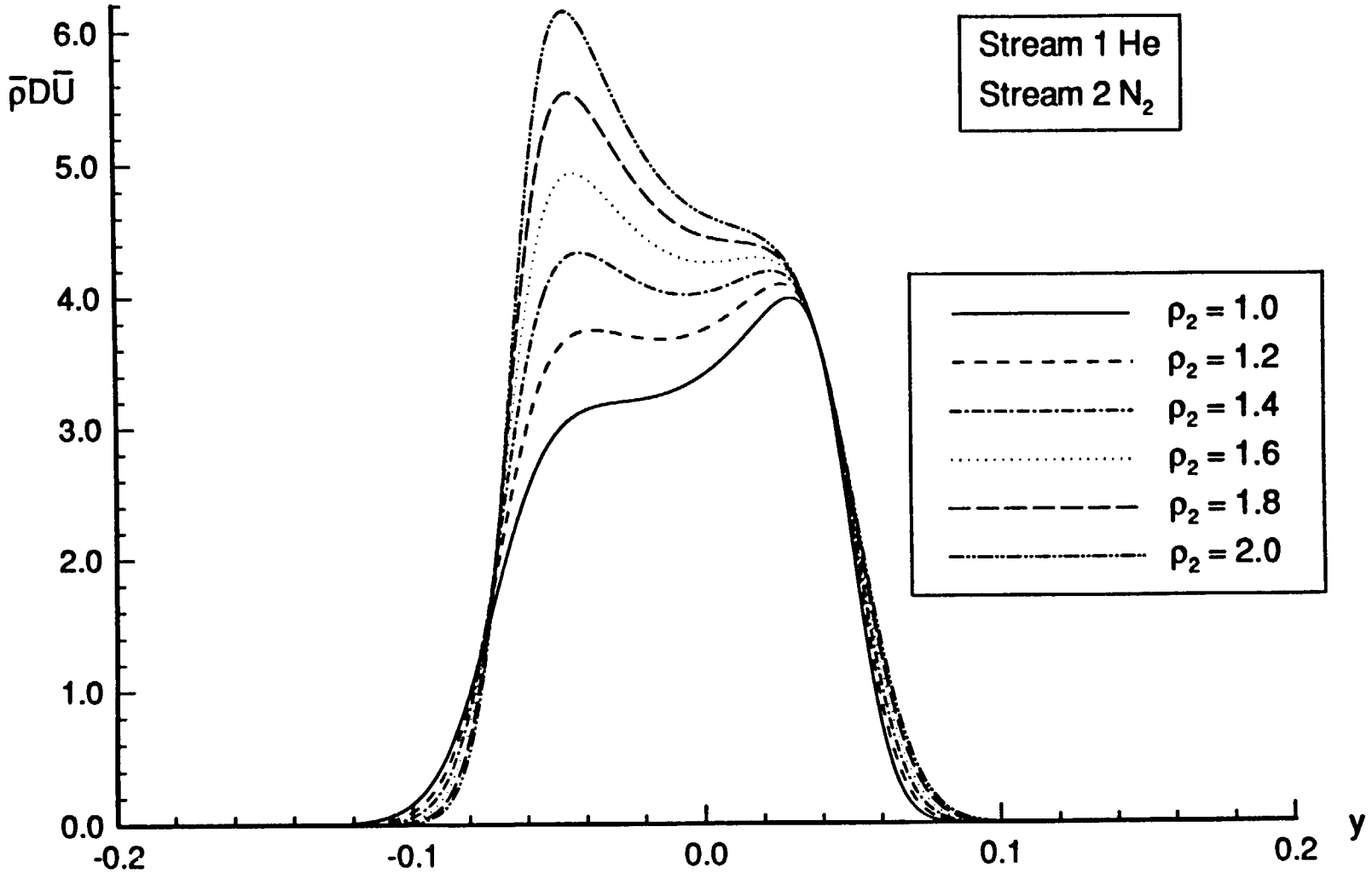
$\bar{\rho}D\bar{U}$
6.0
5.0
4.0
3.0
2.0
1.0
0.0
-0.2
-0.1
0.0
0.1
0.2
y
Stream 1 He
Stream 2 N_2
$\rho_2 = 1.0$
$\rho_2 = 1.2$
$\rho_2 = 1.4$
$\rho_2 = 1.6$
$\rho_2 = 1.8$
$\rho_2 = 2.0$

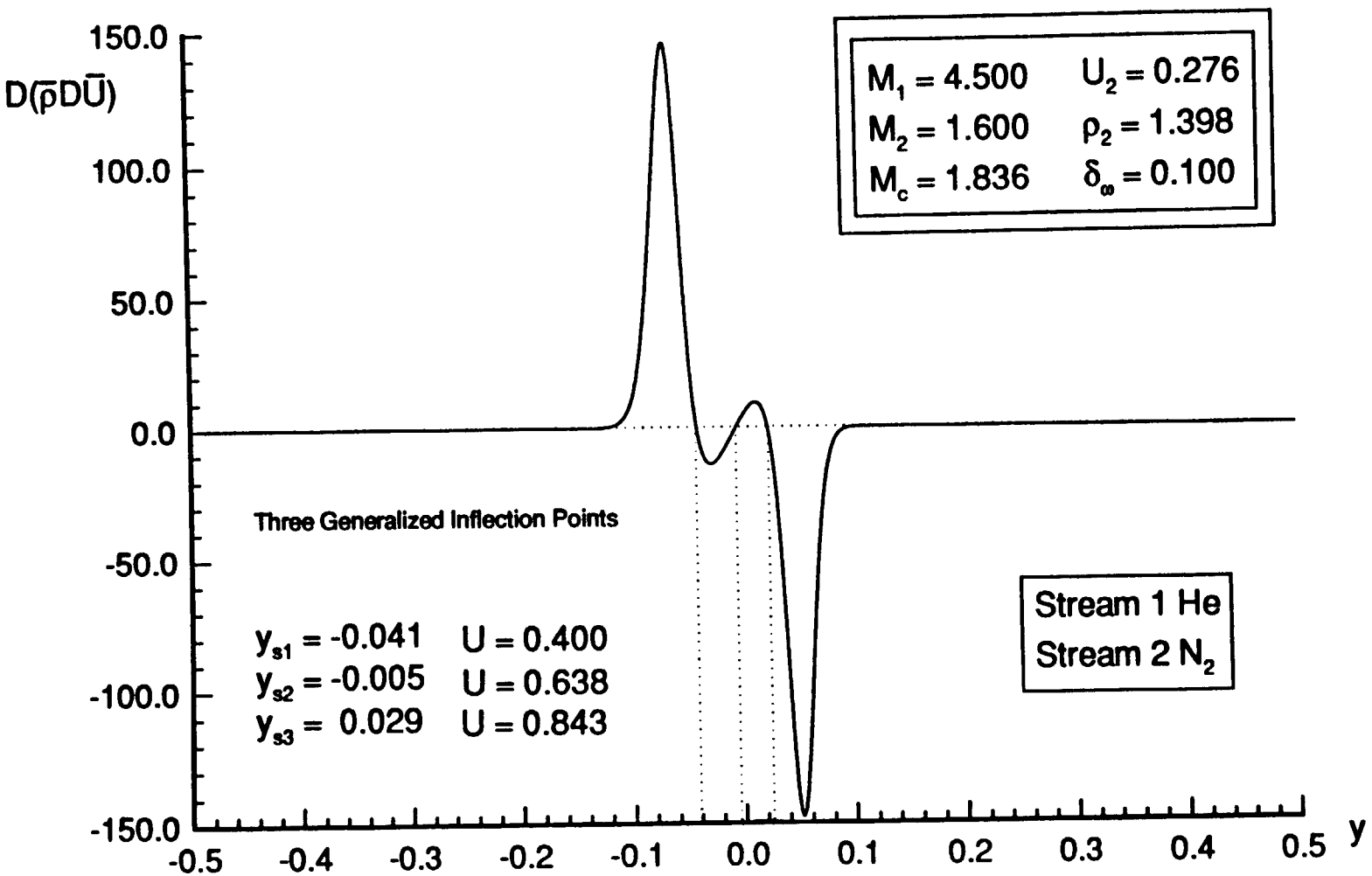
150.0
D(ρ̄DŪ)
100.0
50.0
0.0
-50.0
-100.0
-150.0
-0.5
-0.4
-0.3
-0.2
-0.1
0.0
0.1
0.2
0.3
0.4
0.5
y
M1 = 4.500
U2 = 0.276
M2 = 1.600
ρ2 = 1.398
Mc = 1.836
δω = 0.100
Three Generalized Inflection Points
ys1 = -0.041 U = 0.400
ys2 = -0.005 U = 0.638
ys3 = 0.029 U = 0.843
Stream 1 He
Stream 2 N2

Figure 6

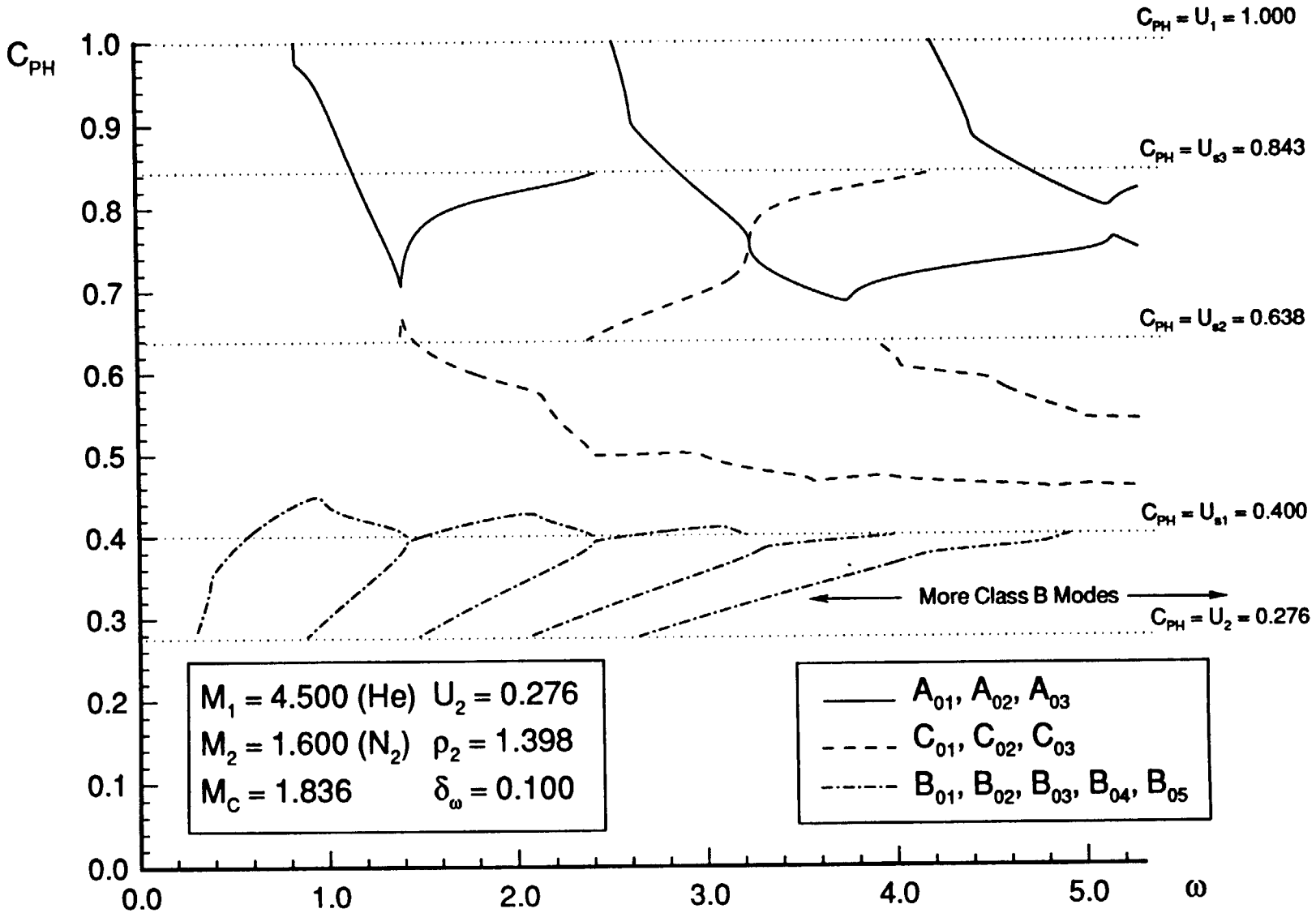
C_{PH}
1.0
0.9
0.8
0.7
0.6
0.5
0.4
0.3
0.2
0.1
0.0
0.0
1.0
2.0
3.0
4.0
5.0
ω
$C_{PH} = U_1 = 1.000$
$C_{PH} = U_{s3} = 0.843$
$C_{PH} = U_{s2} = 0.638$
$C_{PH} = U_{s1} = 0.400$
$C_{PH} = U_2 = 0.276$
More Class B Modes
$M_1 = 4.500$ (He) $U_2 = 0.276$
$M_2 = 1.600$ (N_2) $\rho_2 = 1.398$
$M_C = 1.836$ $\delta_\omega = 0.100$
A_{01}, A_{02}, A_{03}
C_{01}, C_{02}, C_{03}
$B_{01}, B_{02}, B_{03}, B_{04}, B_{05}$

Figure 7

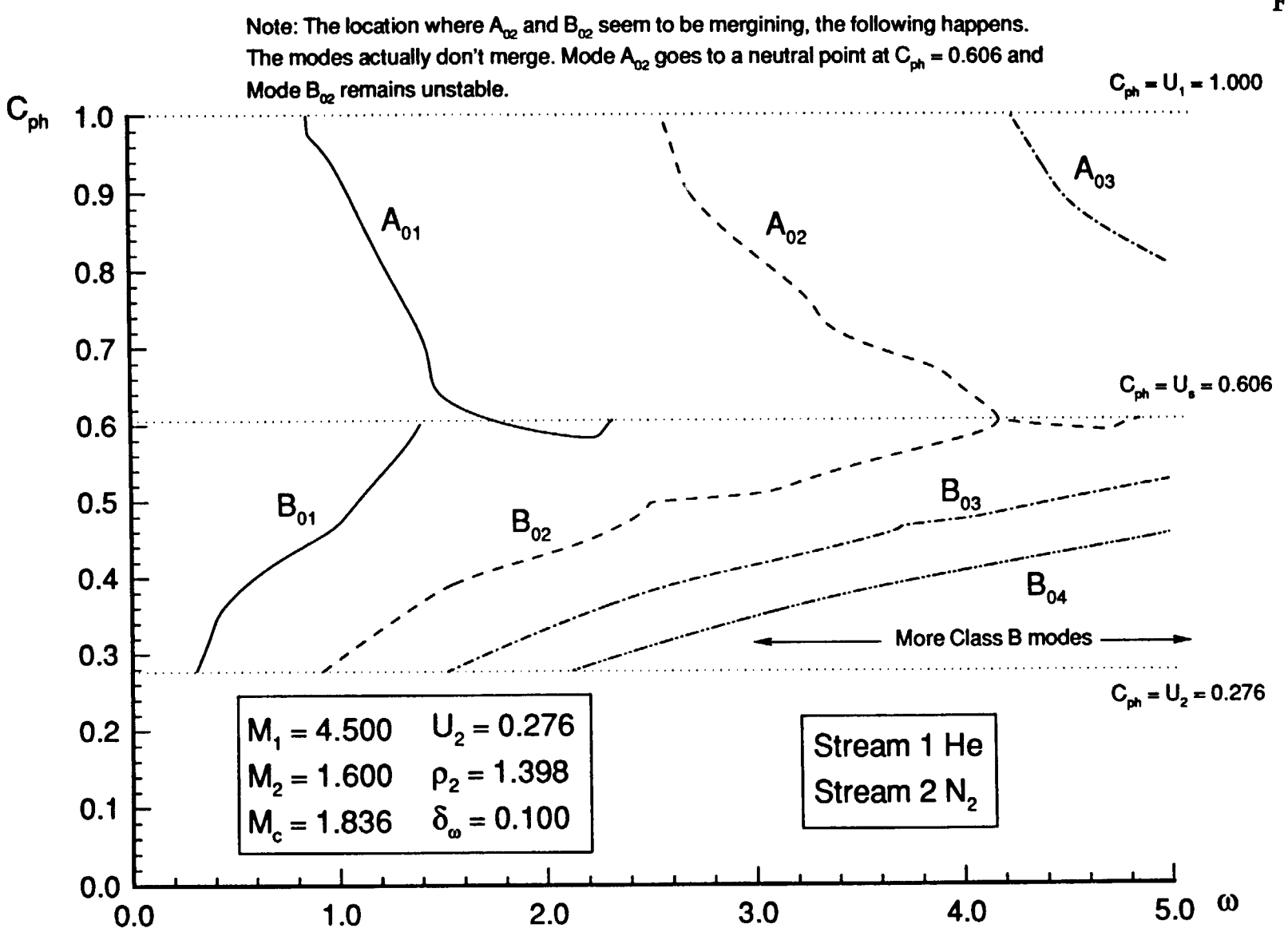
Note: The location where A_{02} and B_{02} seem to be mergining, the following happens.
The modes actually don't merge. Mode A_{02} goes to a neutral point at C_{ph} = 0.606 and
Mode B_{02} remains unstable.
C_{ph}
$C_{ph} = U_1 = 1.000$
$C_{ph} = U_s = 0.606$
$C_{ph} = U_2 = 0.276$
A_{01}
A_{02}
A_{03}
B_{01}
B_{02}
B_{03}
B_{04}
More Class B modes
$M_1 = 4.500$ $U_2 = 0.276$
$M_2 = 1.600$ $\rho_2 = 1.398$
$M_c = 1.836$ $\delta_\omega = 0.100$
Stream 1 He
Stream 2 N_2
0.0
0.1
0.2
0.3
0.4
0.5
0.6
0.7
0.8
0.9
1.0
0.0
1.0
2.0
3.0
4.0
5.0
ω

Figure 8a

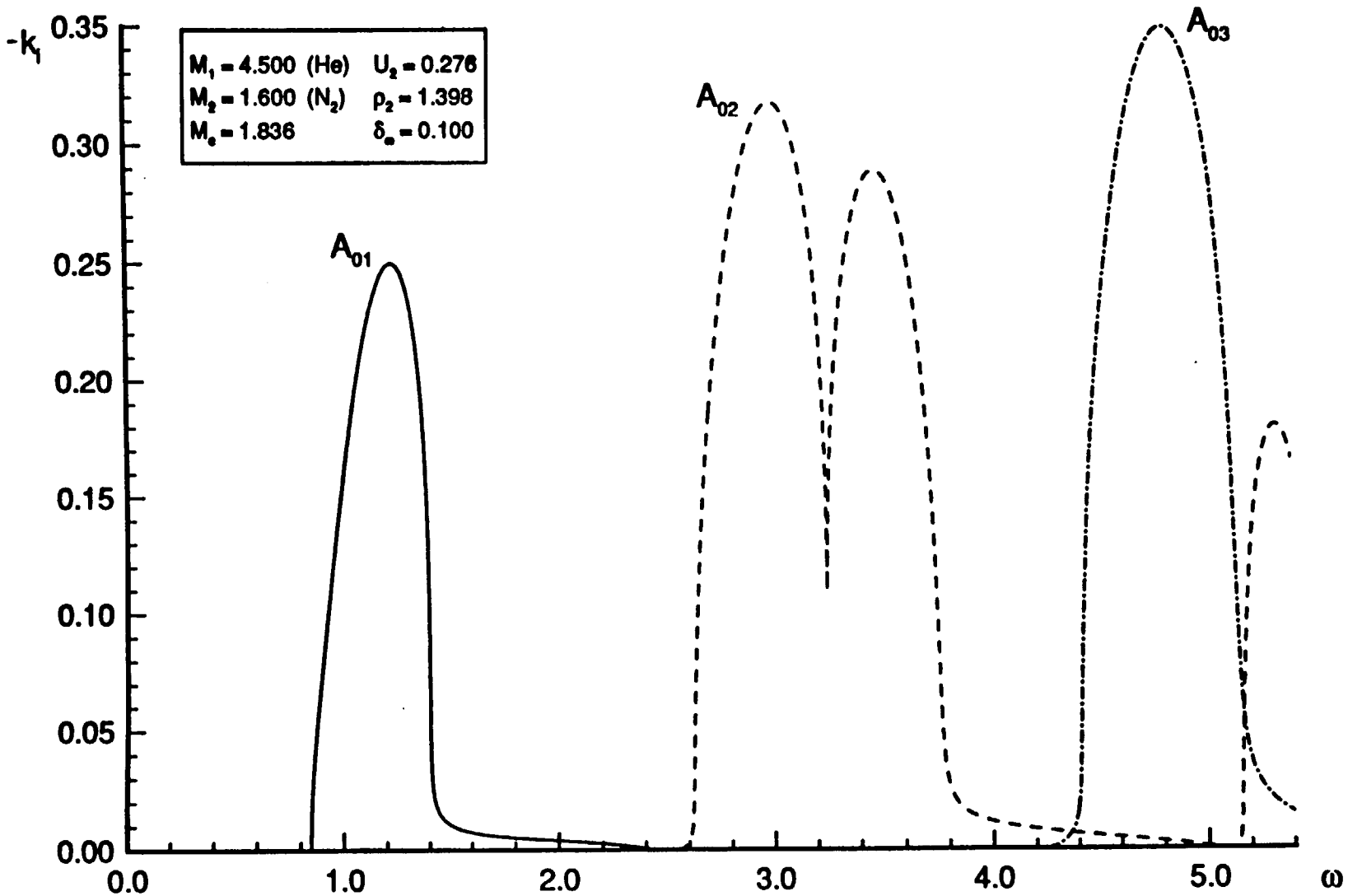
$-k_i$
0.35
0.30
0.25
0.20
0.15
0.10
0.05
0.00
$M_1 = 4.500$ (He) $U_2 = 0.276$
$M_2 = 1.600$ (N_2) $\rho_2 = 1.398$
$M_e = 1.836$ $\delta_e = 0.100$
A_{01}
A_{02}
A_{03}
0.0
1.0
2.0
3.0
4.0
5.0
ω

Figure 8b

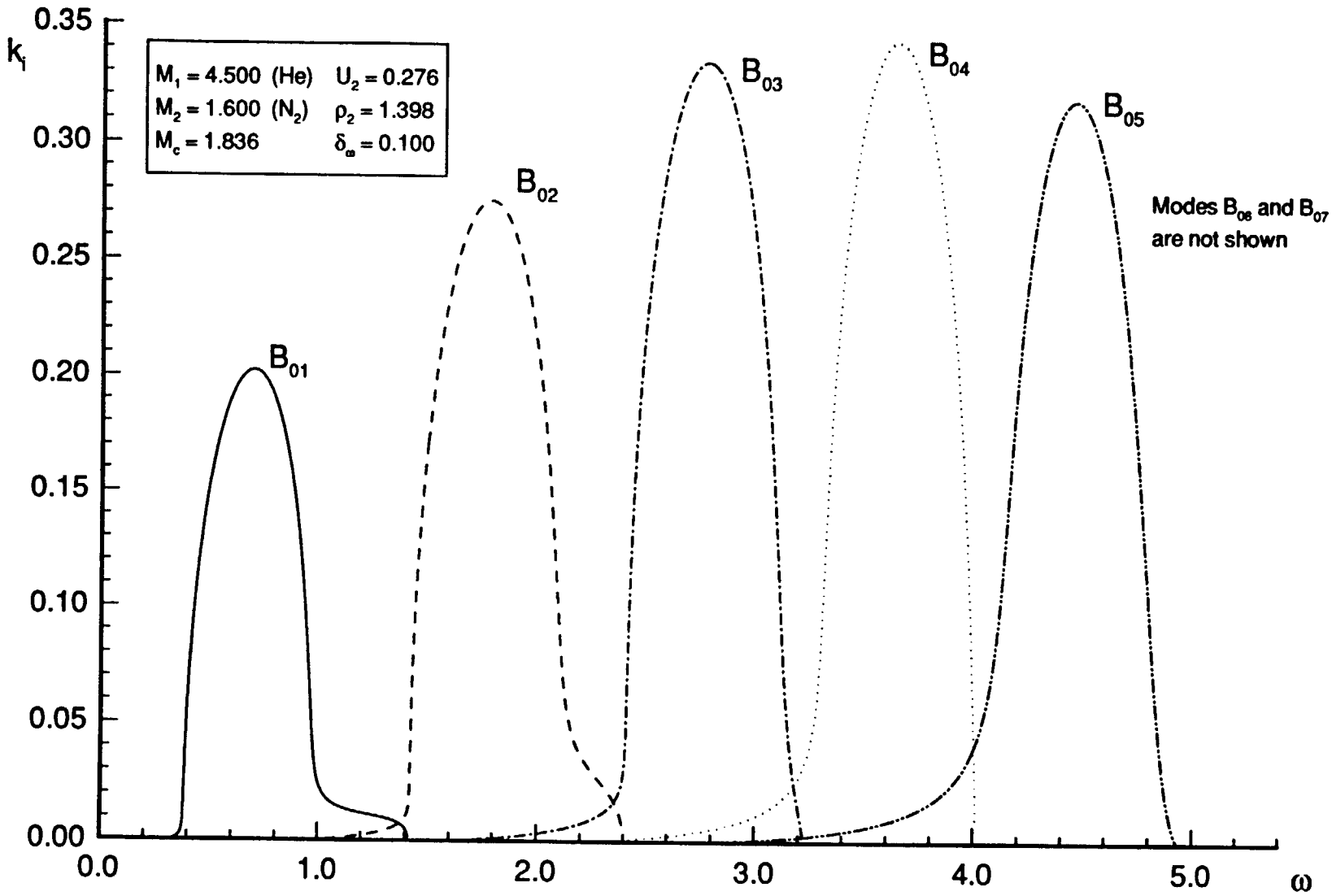
k_i
0.35
0.30
0.25
0.20
0.15
0.10
0.05
0.00
0.0
1.0
2.0
3.0
4.0
5.0
ω
$M_1 = 4.500$ (He) $U_2 = 0.276$
$M_2 = 1.600$ (N_2) $\rho_2 = 1.398$
$M_c = 1.836$ $\delta_\omega = 0.100$
B_{01}
B_{02}
B_{03}
B_{04}
B_{05}
Modes B_{06} and B_{07} are not shown

Figure 8c

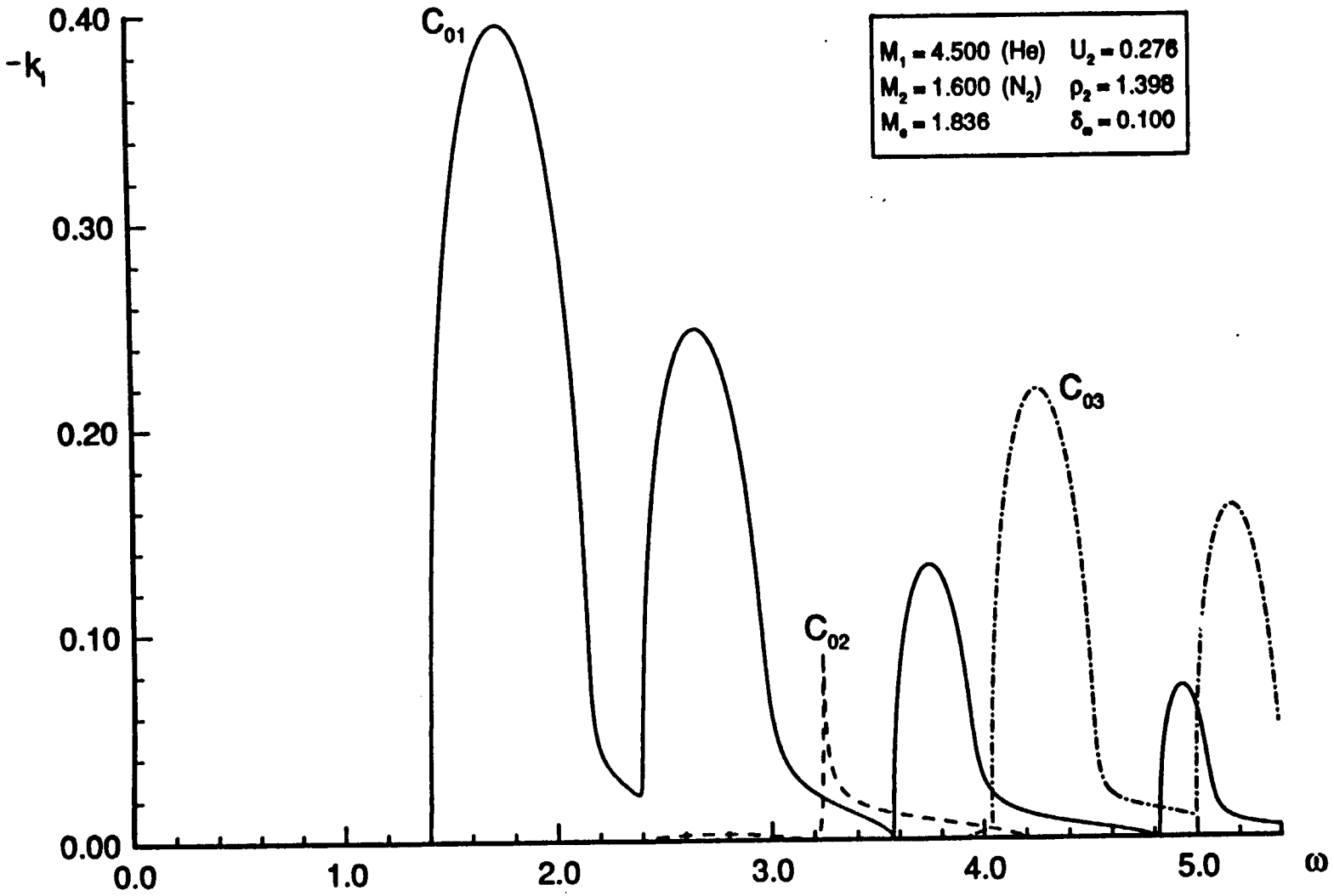
0.40
$-k_1$
0.30
0.20
0.10
0.00
0.0
1.0
2.0
3.0
4.0
5.0
ω
C_{01}
C_{02}
C_{03}
$M_1 = 4.500$ (He) $U_2 = 0.276$
$M_2 = 1.600$ (N_2) $\rho_2 = 1.398$
$M_e = 1.836$ $\delta_e = 0.100$

Figure 9a

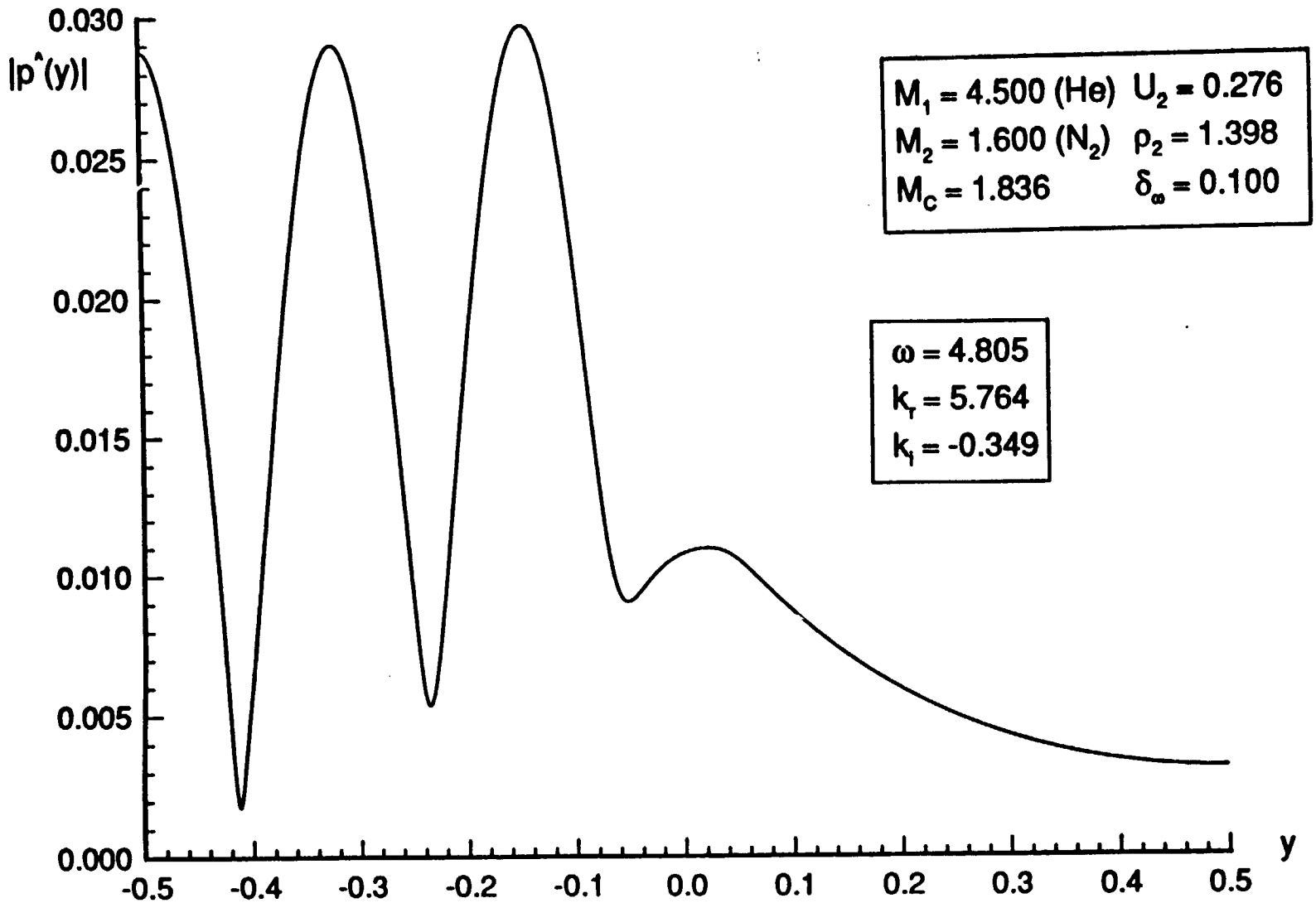
0.030
|p^(y)|
0.025
0.020
0.015
0.010
0.005
0.000
-0.5
-0.4
-0.3
-0.2
-0.1
0.0
0.1
0.2
0.3
0.4
0.5
y
M1 = 4.500 (He) U2 = 0.276
M2 = 1.600 (N2) ρ2 = 1.398
Mc = 1.836 δω = 0.100
ω = 4.805
kr = 5.764
ki = -0.349

Figure 9b

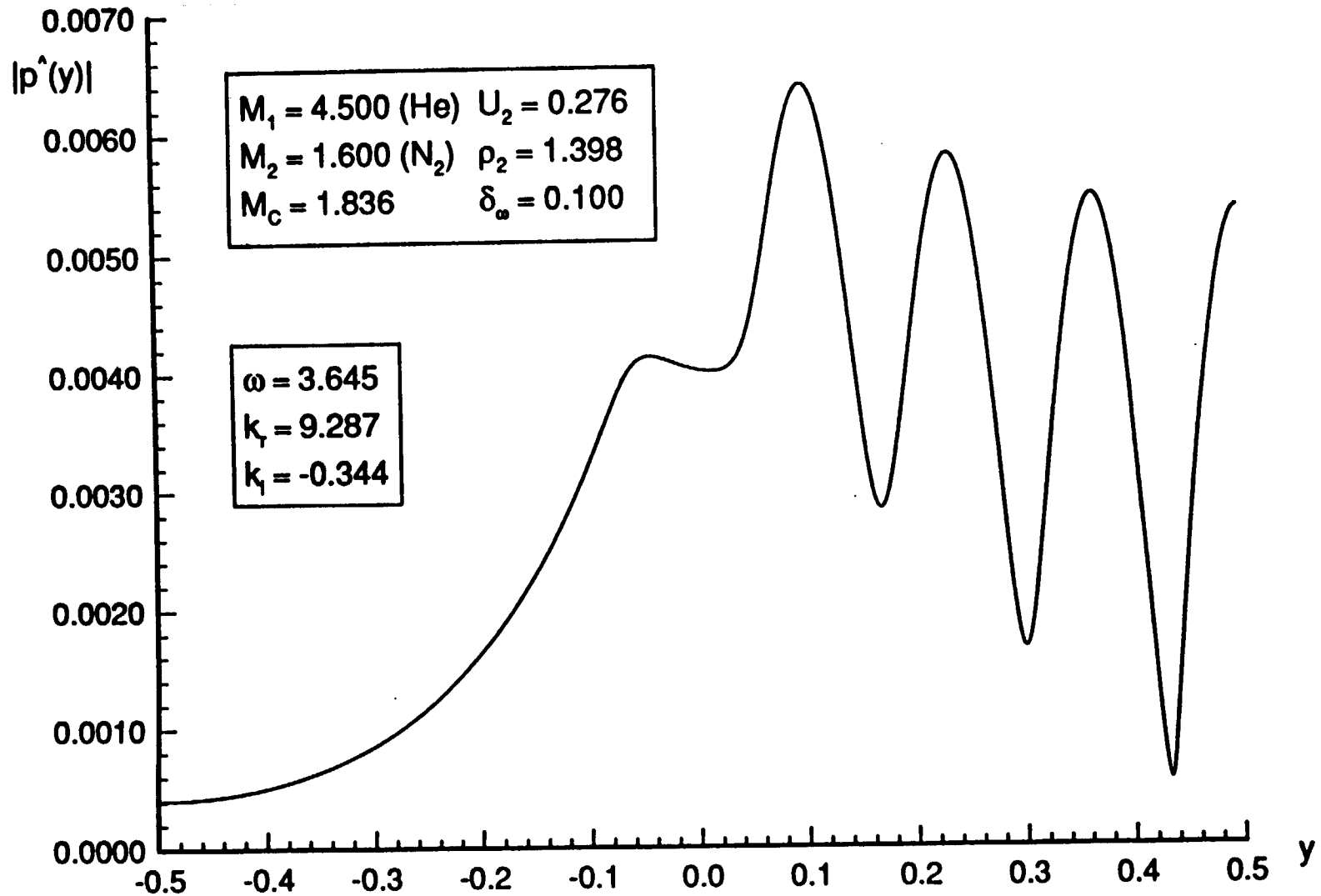
0.0070
|p^(y)|
0.0060
0.0050
0.0040
0.0030
0.0020
0.0010
0.0000
M1 = 4.500 (He) U2 = 0.276
M2 = 1.600 (N2) ρ2 = 1.398
Mc = 1.836 δω = 0.100
ω = 3.645
kr = 9.287
ki = -0.344
-0.5
-0.4
-0.3
-0.2
-0.1
0.0
0.1
0.2
0.3
0.4
0.5
y

Figure 9c

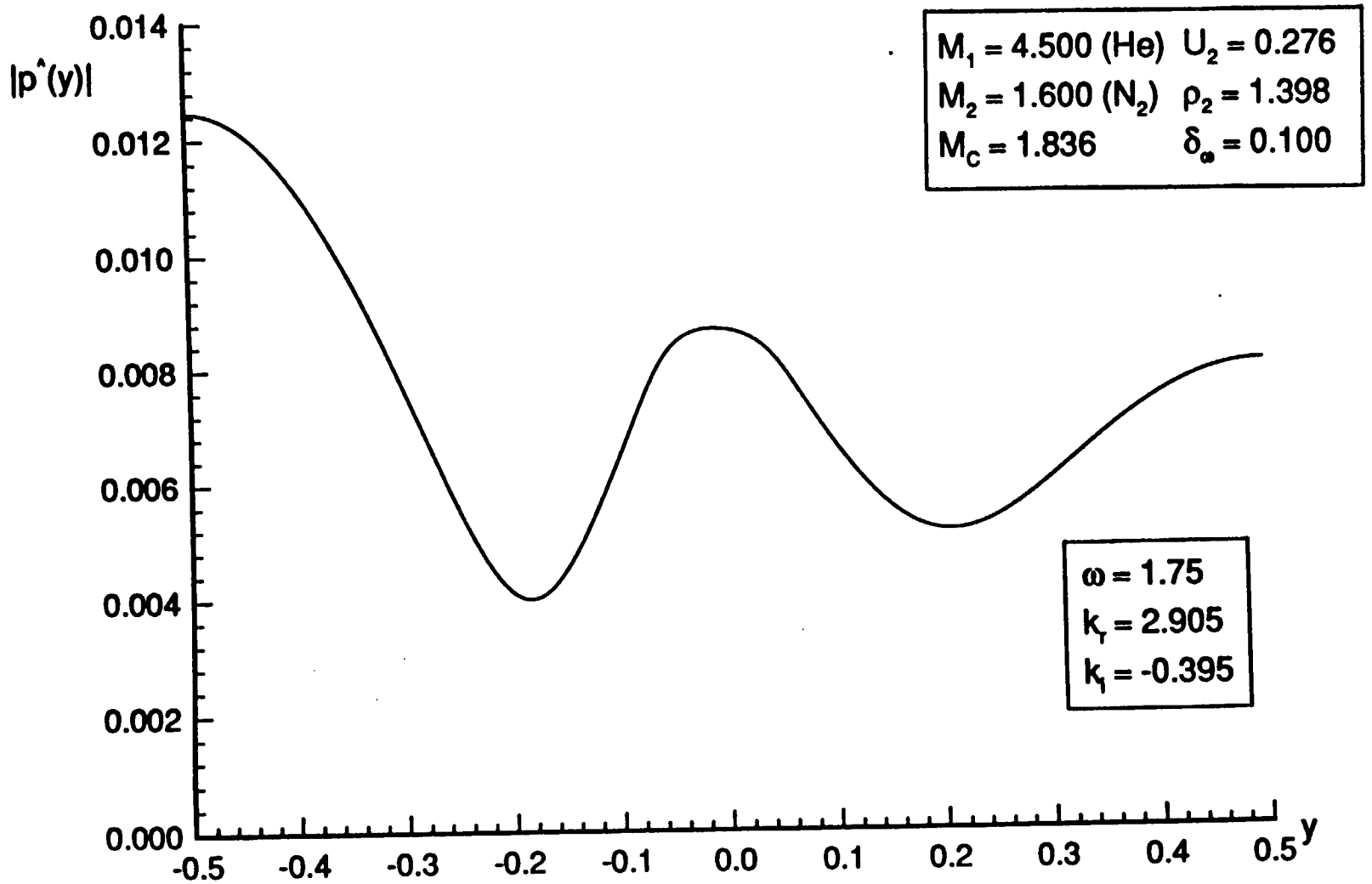
|p^(y)|
0.014
0.012
0.010
0.008
0.006
0.004
0.002
0.000
-0.5
-0.4
-0.3
-0.2
-0.1
0.0
0.1
0.2
0.3
0.4
0.5
y
M1 = 4.500 (He) U2 = 0.276
M2 = 1.600 (N2) ρ2 = 1.398
Mc = 1.836 δω = 0.100
ω = 1.75
kr = 2.905
ki = -0.395

Figure 10

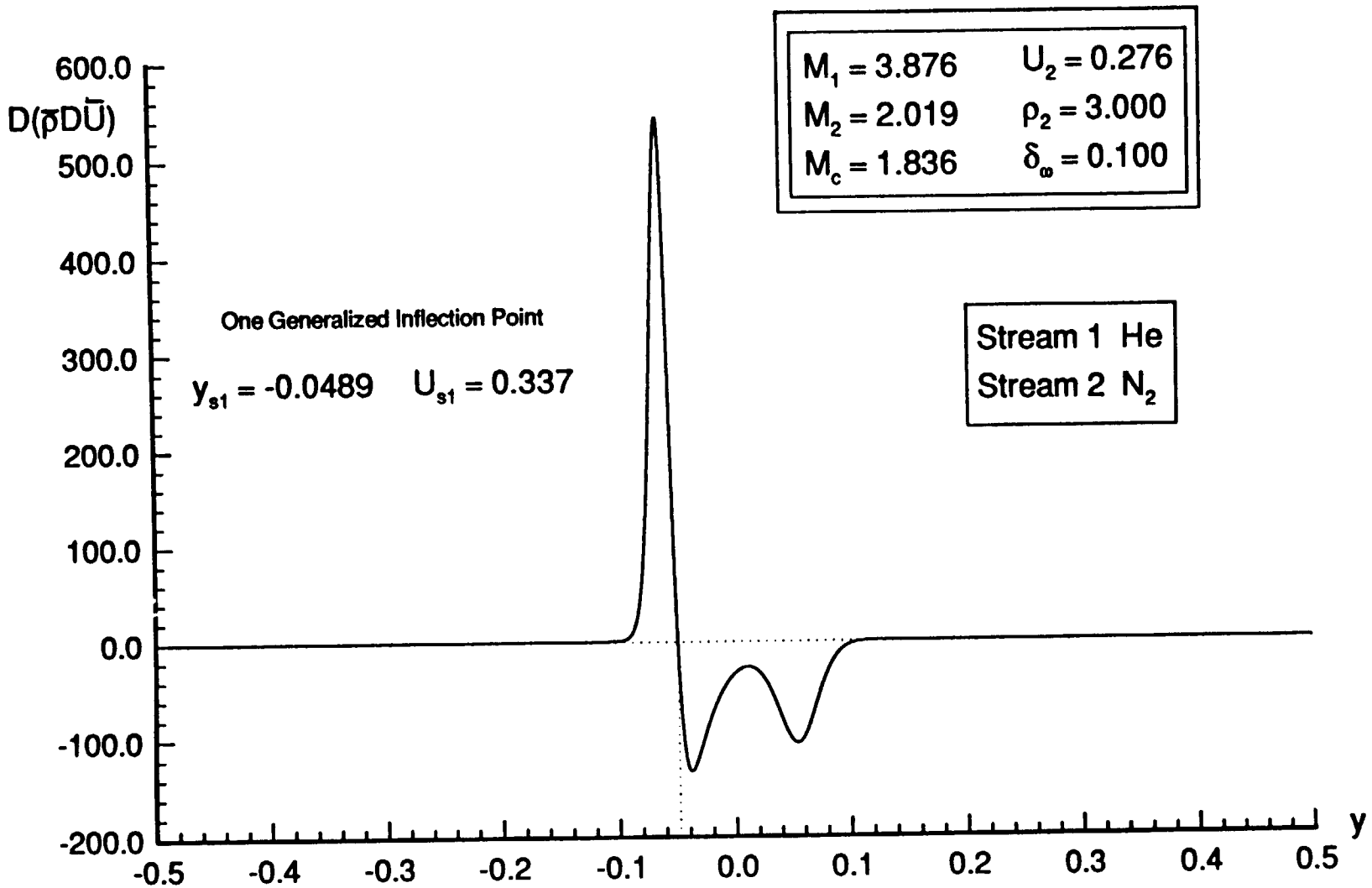
$M_1 = 3.876$ $U_2 = 0.276$
$M_2 = 2.019$ $\rho_2 = 3.000$
$M_c = 1.836$ $\delta_\omega = 0.100$
Stream 1 He
Stream 2 N_2
One Generalized Inflection Point
$y_{s1} = -0.0489$ $U_{s1} = 0.337$
$D(\bar{\rho}D\tilde{U})$
600.0
500.0
400.0
300.0
200.0
100.0
0.0
-100.0
-200.0
-0.5
-0.4
-0.3
-0.2
-0.1
0.0
0.1
0.2
0.3
0.4
0.5
y

Figure 11

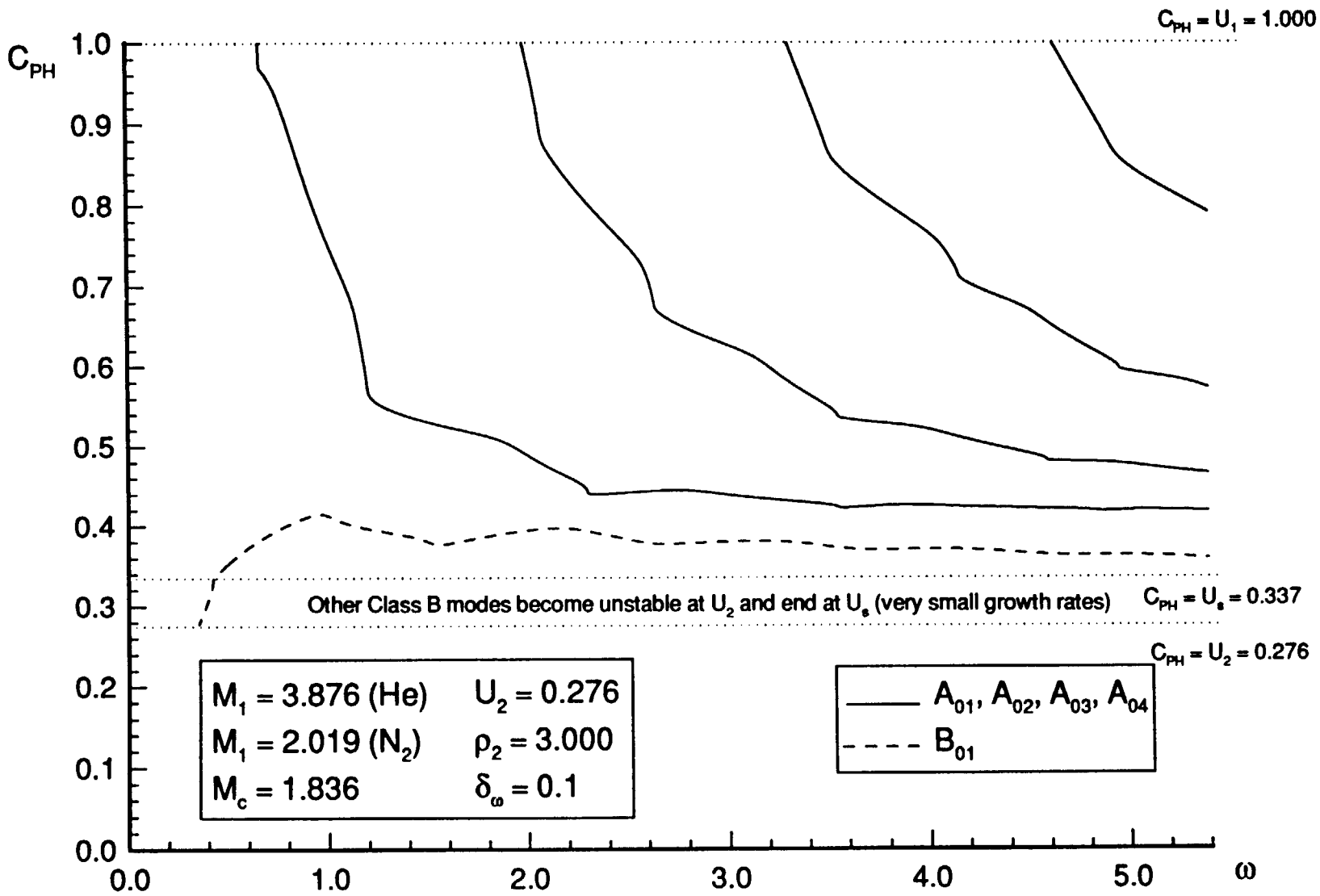
$C_{PH} = U_1 = 1.000$
C_{PH}
1.0
0.9
0.8
0.7
0.6
0.5
0.4
0.3
0.2
0.1
0.0
Other Class B modes become unstable at U_2 and end at U_s (very small growth rates)
$C_{PH} = U_s = 0.337$
$C_{PH} = U_2 = 0.276$
$M_1 = 3.876$ (He) $U_2 = 0.276$
$M_1 = 2.019$ (N_2) $\rho_2 = 3.000$
$M_c = 1.836$ $\delta_\omega = 0.1$
A_{01}, A_{02}, A_{03}, A_{04}
B_{01}
0.0
1.0
2.0
3.0
4.0
5.0
ω

Figure 12a

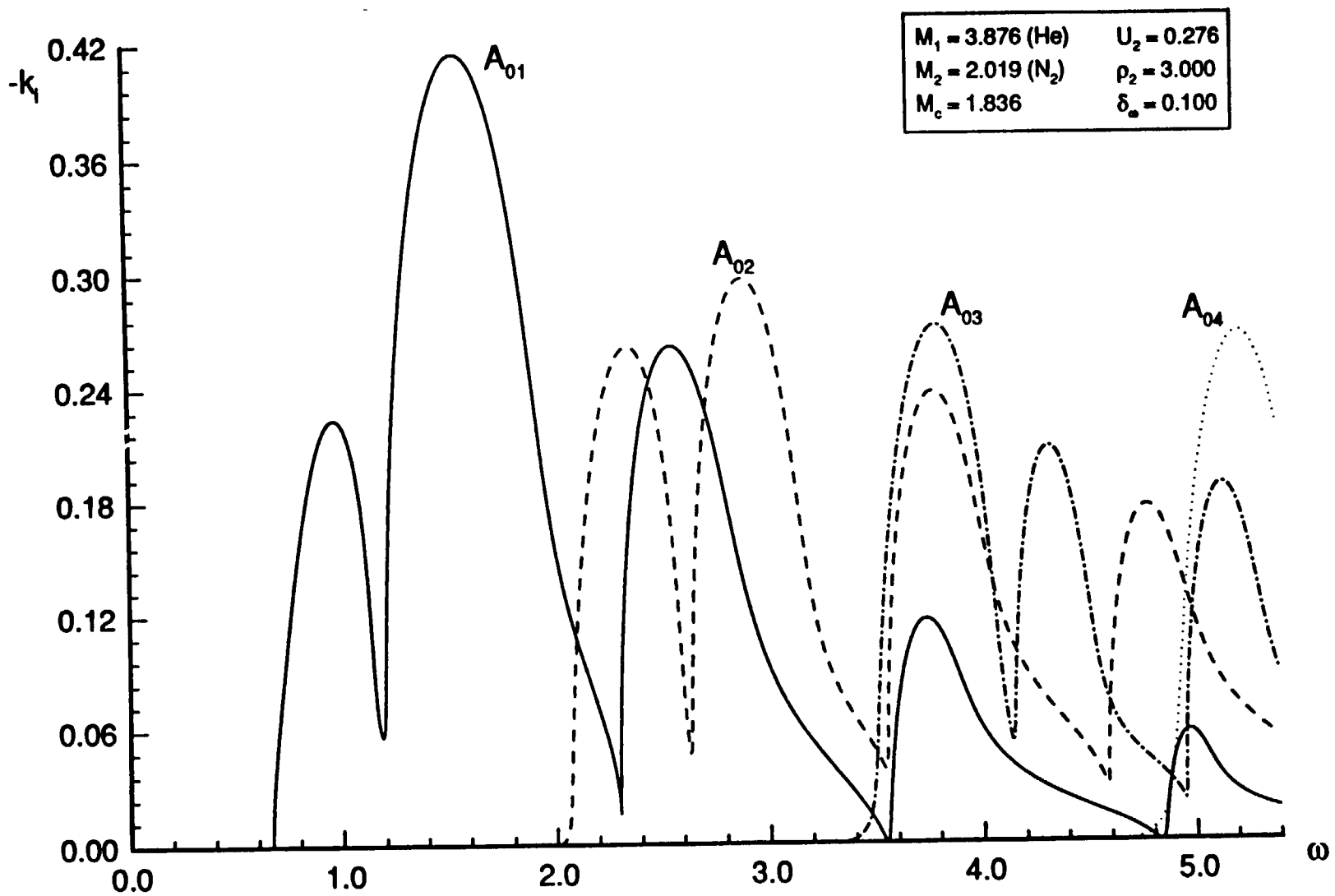
$M_1 = 3.876$ (He)
$U_2 = 0.276$
$M_2 = 2.019$ (N_2)
$\rho_2 = 3.000$
$M_c = 1.836$
$\delta_\omega = 0.100$
$-k_i$
0.42
0.36
0.30
0.24
0.18
0.12
0.06
0.00
A_{01}
A_{02}
A_{03}
A_{04}
0.0
1.0
2.0
3.0
4.0
5.0
ω

Figure 12b

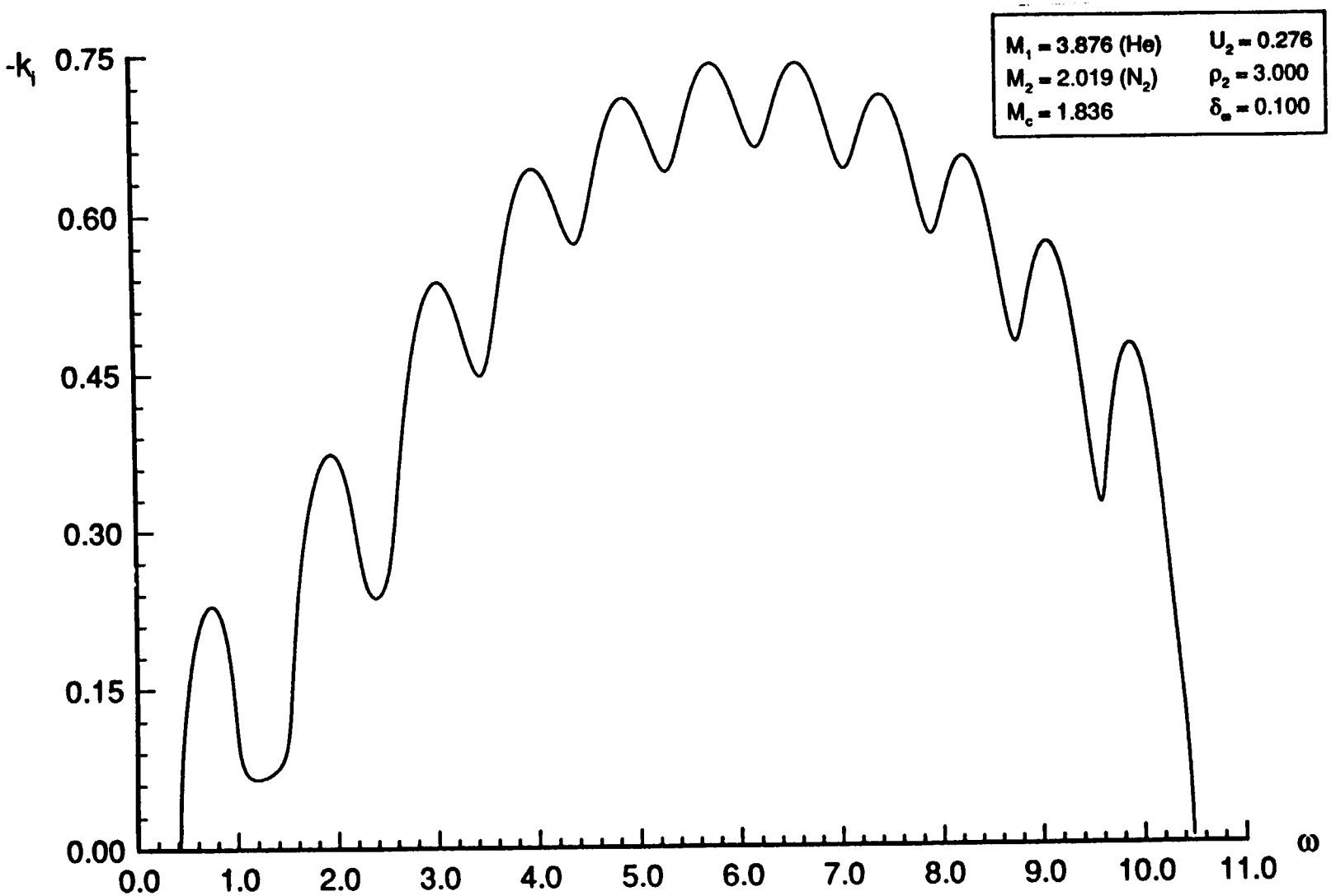
$M_1 = 3.876$ (He)
$M_2 = 2.019$ (N_2)
$M_c = 1.836$
$U_2 = 0.276$
$\rho_2 = 3.000$
$\delta_\omega = 0.100$
$-k_i$
0.75
0.60
0.45
0.30
0.15
0.00
0.0
1.0
2.0
3.0
4.0
5.0
6.0
7.0
8.0
9.0
10.0
11.0
ω

Figure 13

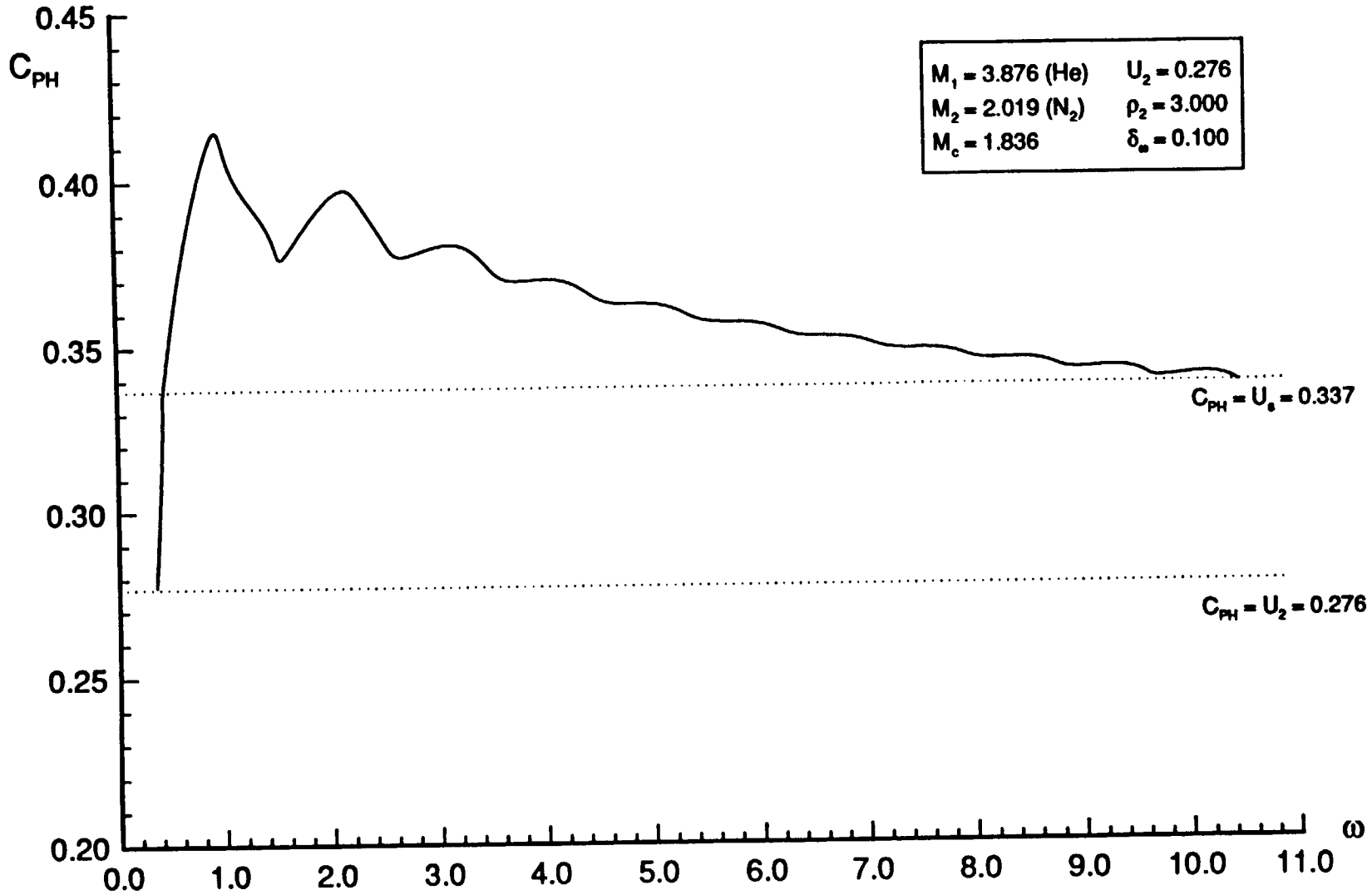
0.45
C_{PH}
0.40
0.35
0.30
0.25
0.20
0.0
1.0
2.0
3.0
4.0
5.0
6.0
7.0
8.0
9.0
10.0
11.0
ω
$M_1 = 3.876$ (He)
$U_2 = 0.276$
$M_2 = 2.019$ (N_2)
$\rho_2 = 3.000$
$M_c = 1.836$
$\delta_\omega = 0.100$
$C_{PH} = U_c = 0.337$
$C_{PH} = U_2 = 0.276$

Figure 14a

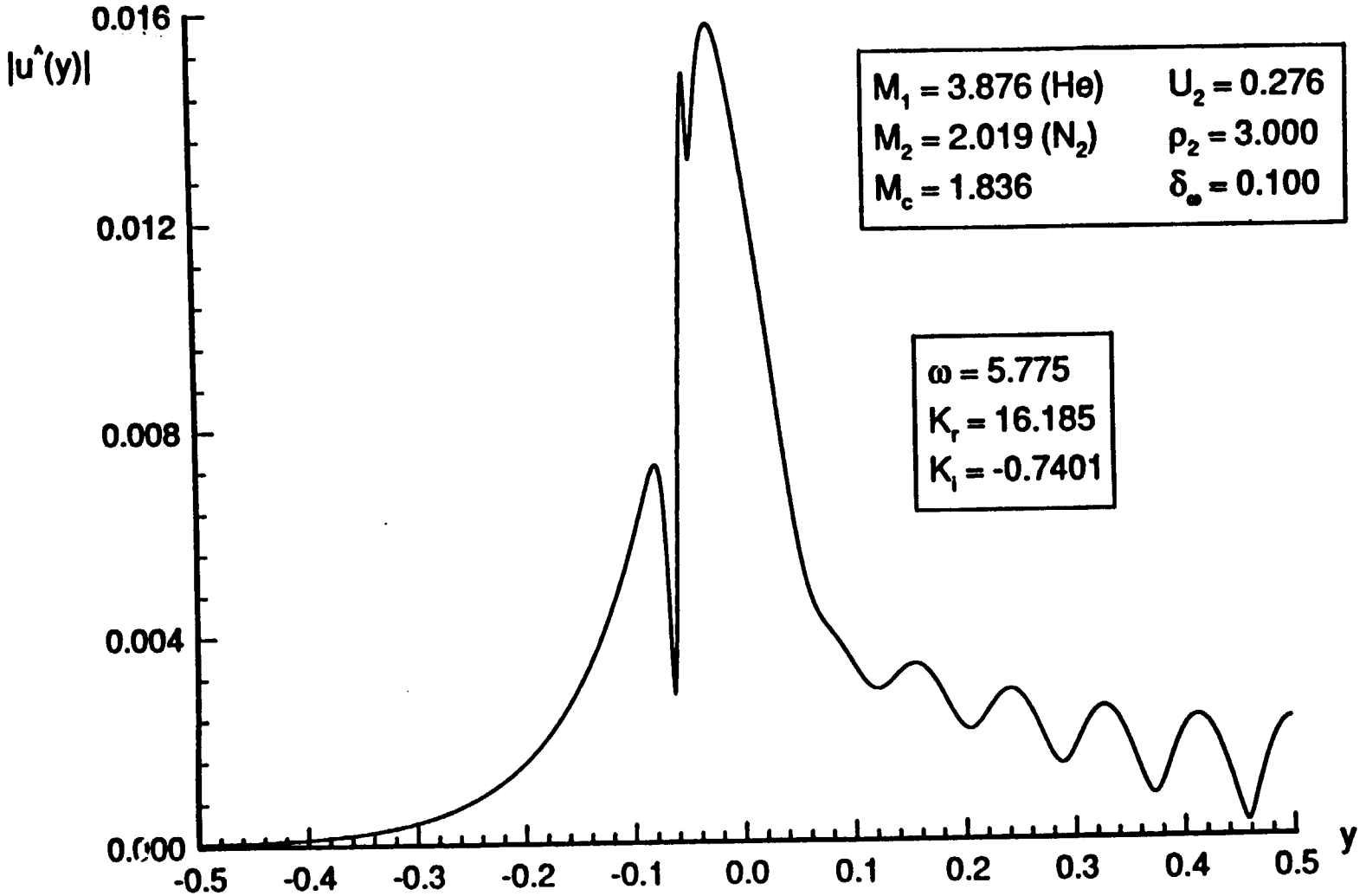
0.016
|u^(y)|
0.012
0.008
0.004
0.000
-0.5
-0.4
-0.3
-0.2
-0.1
0.0
0.1
0.2
0.3
0.4
0.5
y
M1 = 3.876 (Hθ)
U2 = 0.276
M2 = 2.019 (N2)
ρ2 = 3.000
Mc = 1.836
δω = 0.100
ω = 5.775
Kr = 16.185
Ki = -0.7401

Figure 14b

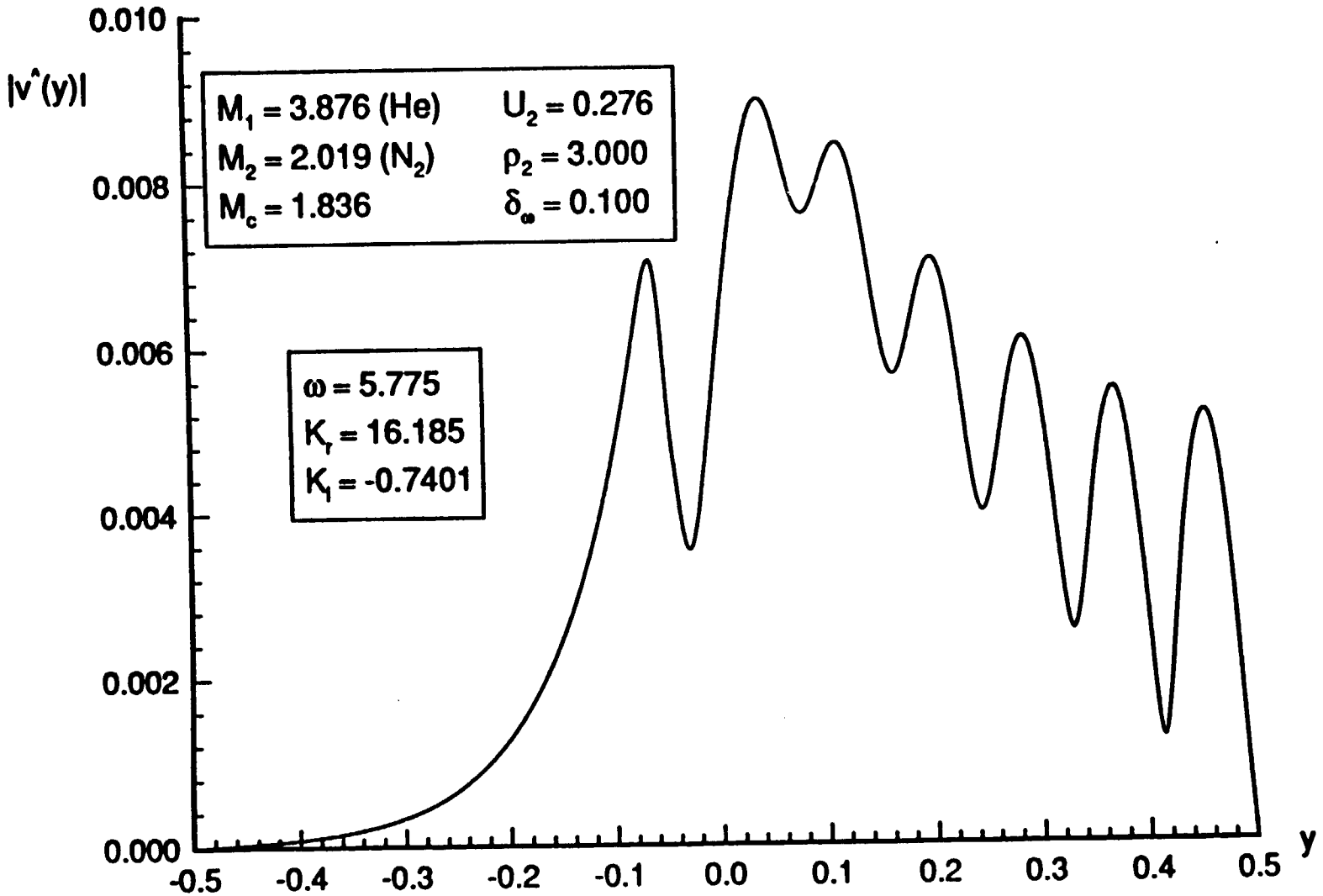
0.010
|v^(y)|
0.008
0.006
0.004
0.002
0.000
M1 = 3.876 (He)
M2 = 2.019 (N2)
Mc = 1.836
U2 = 0.276
ρ2 = 3.000
δ∞ = 0.100
ω = 5.775
Kr = 16.185
Ki = -0.7401
-0.5
-0.4
-0.3
-0.2
-0.1
0.0
0.1
0.2
0.3
0.4
0.5
y

Figure 14c

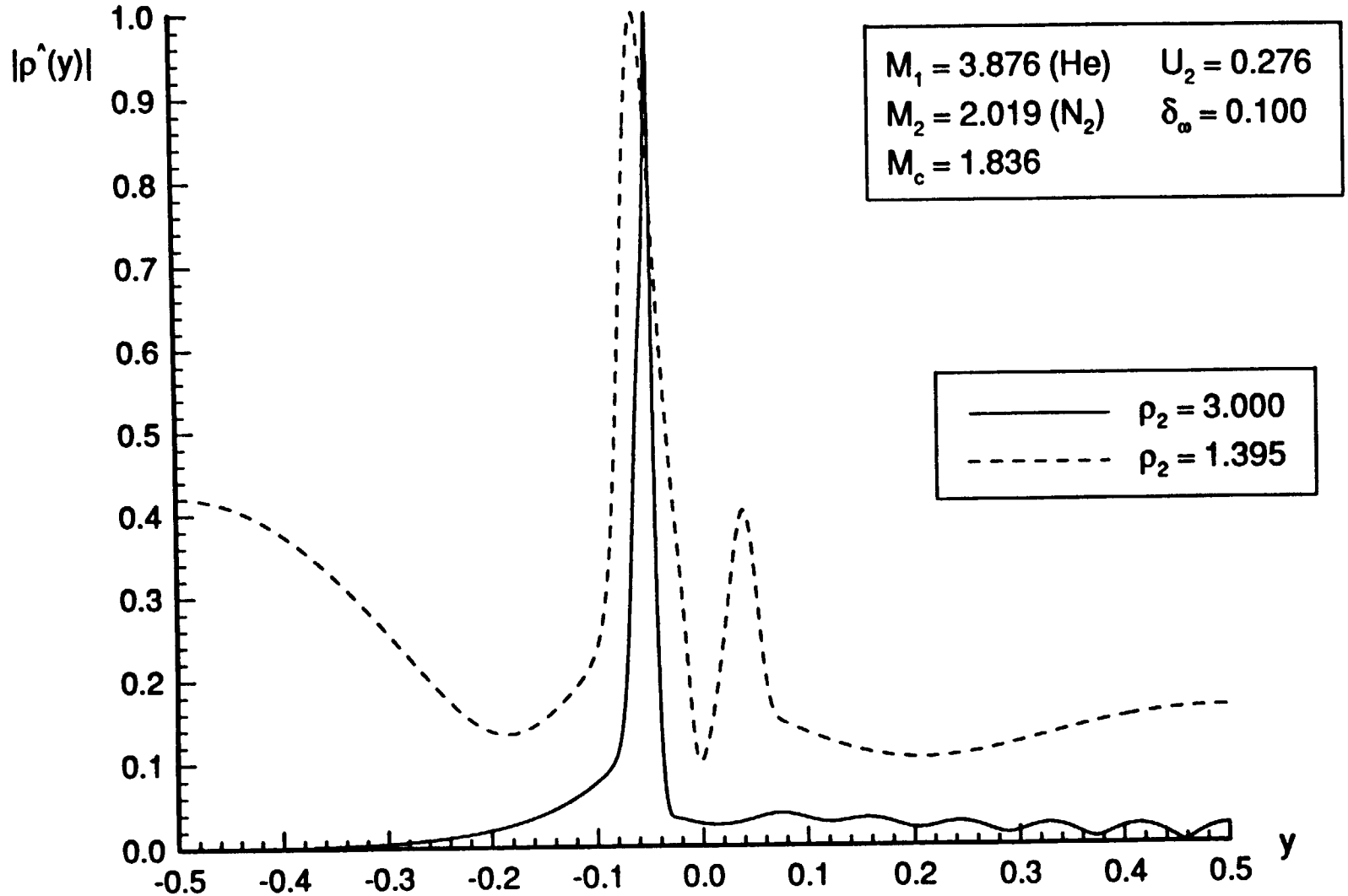
|ρ^(y)|
1.0
0.9
0.8
0.7
0.6
0.5
0.4
0.3
0.2
0.1
0.0
-0.5
-0.4
-0.3
-0.2
-0.1
0.0
0.1
0.2
0.3
0.4
0.5
y
M1 = 3.876 (He)
U2 = 0.276
M2 = 2.019 (N2)
δω = 0.100
Mc = 1.836
ρ2 = 3.000
ρ2 = 1.395

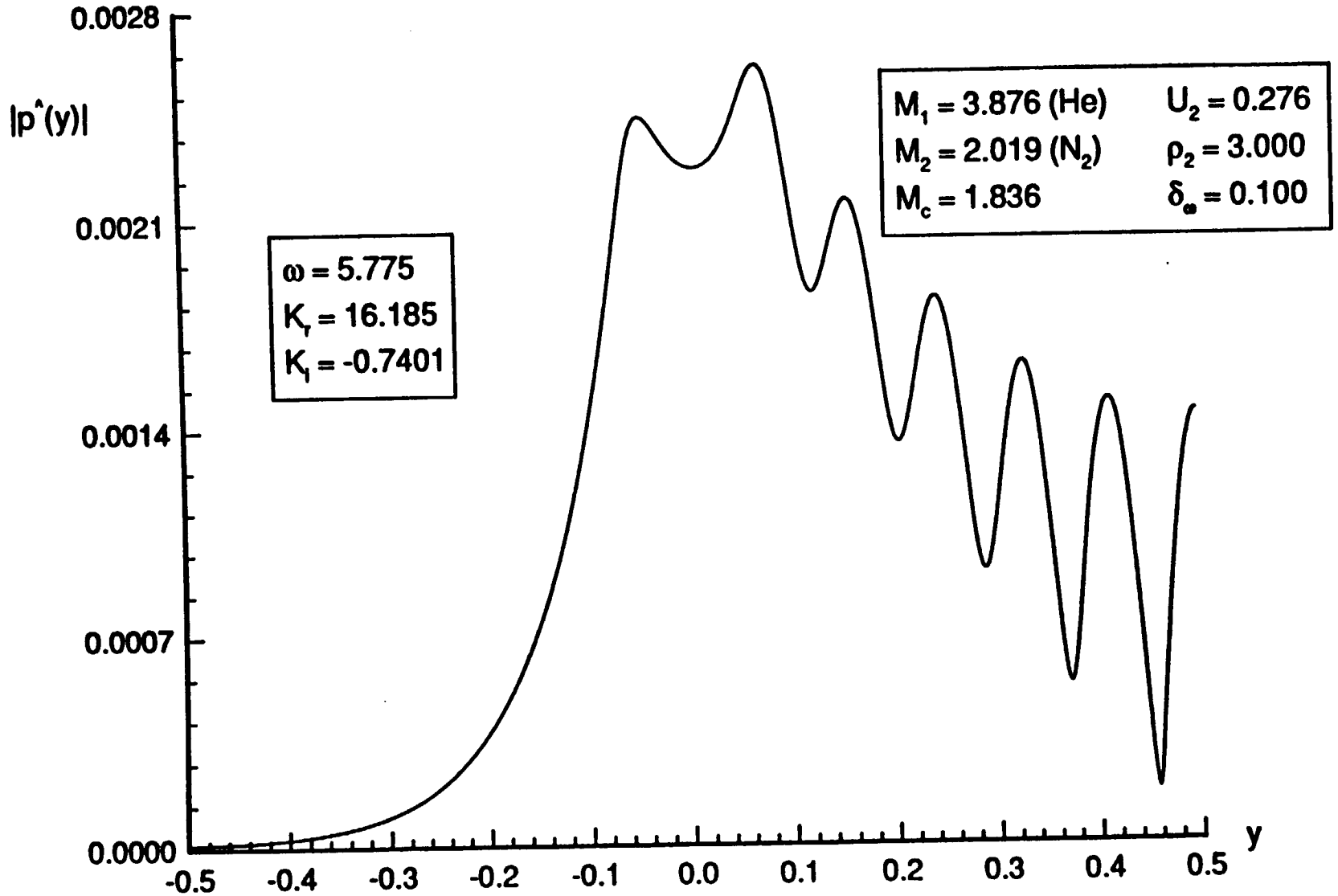
0.0028
|p^(y)|
0.0021
0.0014
0.0007
0.0000
-0.5
-0.4
-0.3
-0.2
-0.1
0.0
0.1
0.2
0.3
0.4
0.5
y
ω = 5.775
K_r = 16.185
K_i = -0.7401
M_1 = 3.876 (He)
M_2 = 2.019 (N_2)
M_c = 1.836
U_2 = 0.276
ρ_2 = 3.000
δ_ω = 0.100

Figure 14e

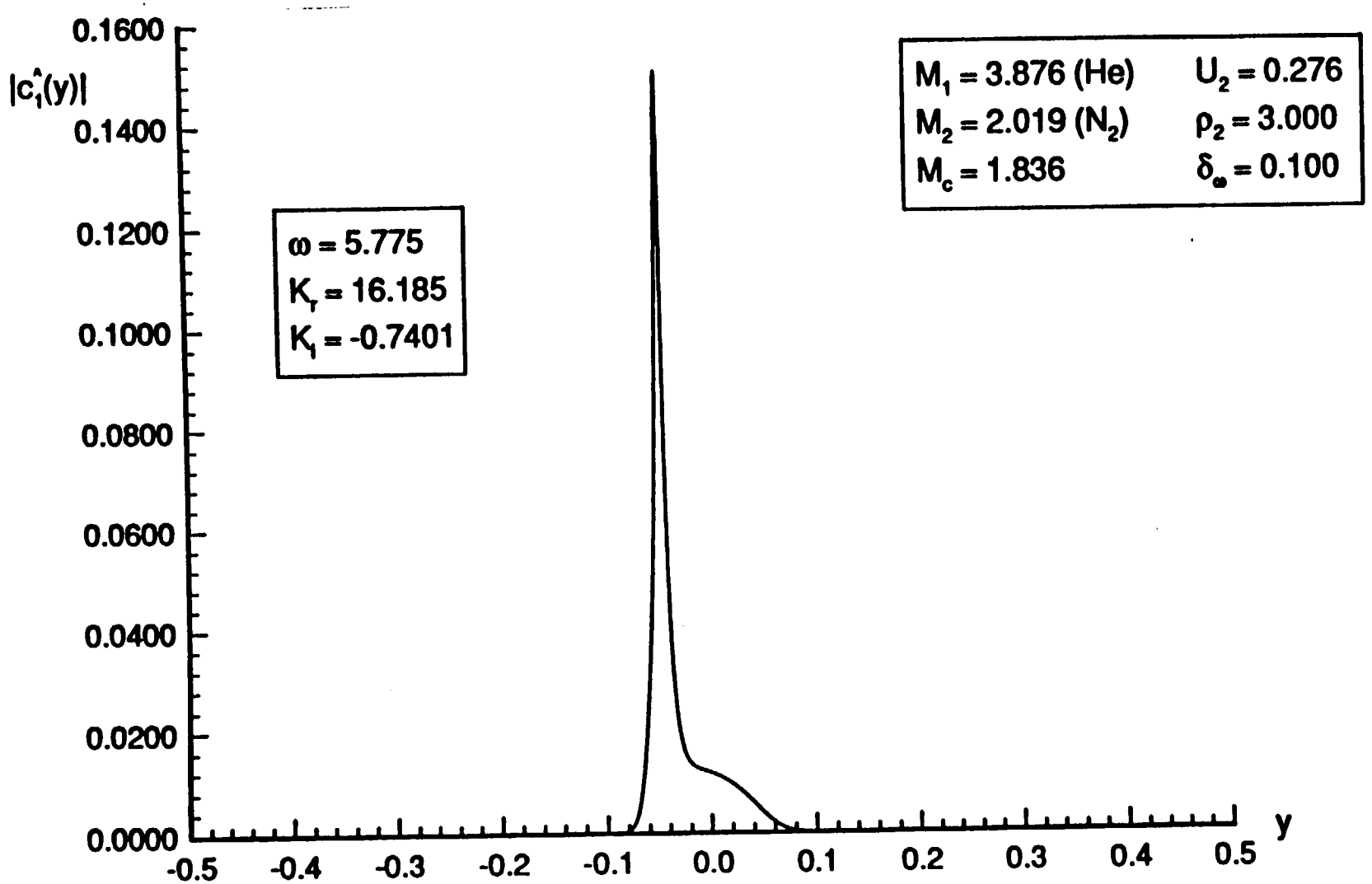
0.1600
|c1^(y)|
0.1400
0.1200
0.1000
0.0800
0.0600
0.0400
0.0200
0.0000
-0.5
-0.4
-0.3
-0.2
-0.1
0.0
0.1
0.2
0.3
0.4
0.5
y
ω = 5.775
Kr = 16.185
Ki = -0.7401
M1 = 3.876 (He)
M2 = 2.019 (N2)
Mc = 1.836
U2 = 0.276
ρ2 = 3.000
δω = 0.100

Figure 15

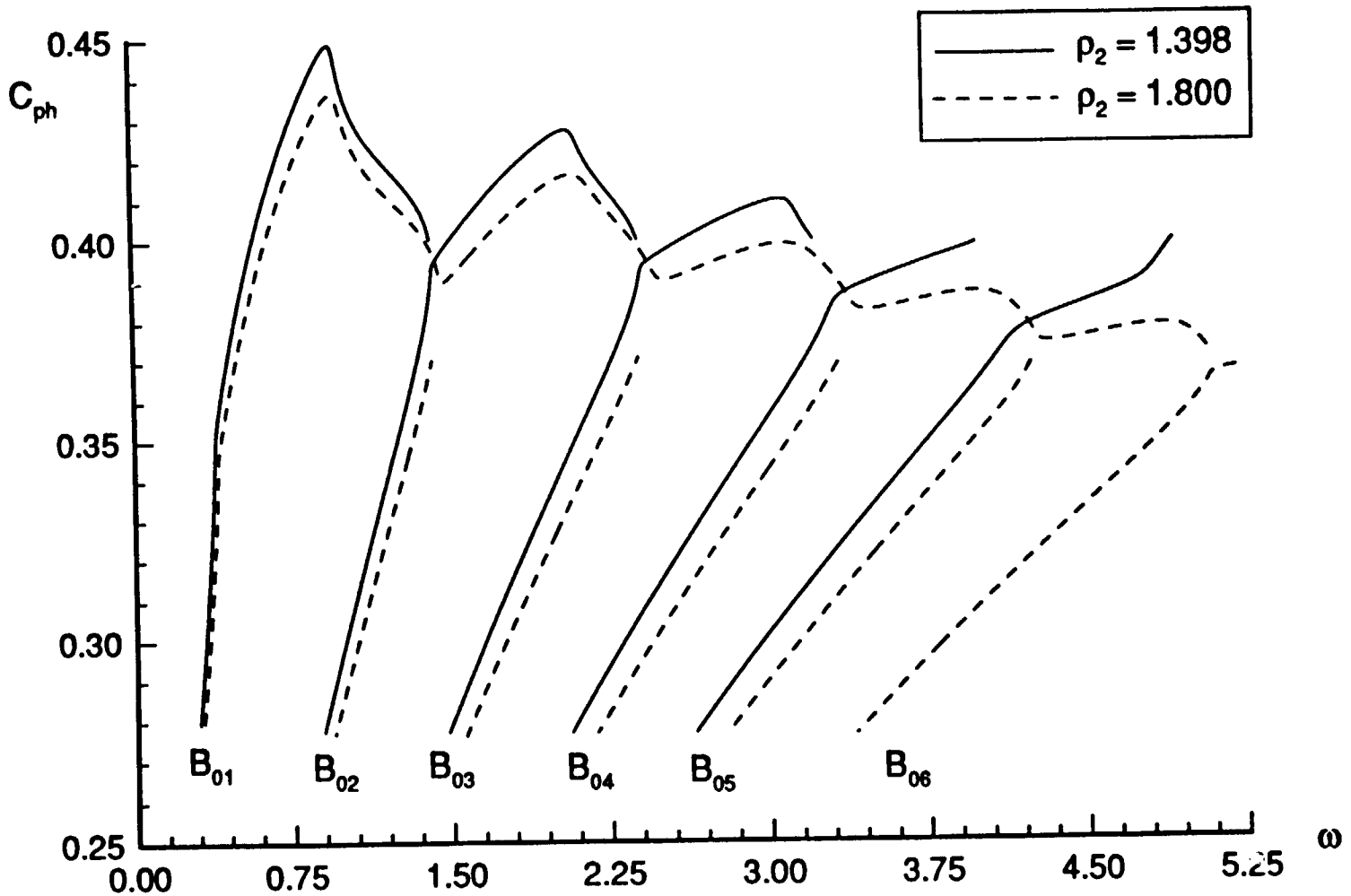
0.45
C_{ph}
0.40
0.35
0.30
0.25
0.00
0.75
1.50
2.25
3.00
3.75
4.50
5.25
ω
$\rho_2 = 1.398$
$\rho_2 = 1.800$
B_{01}
B_{02}
B_{03}
B_{04}
B_{05}
B_{06}

Figure 16

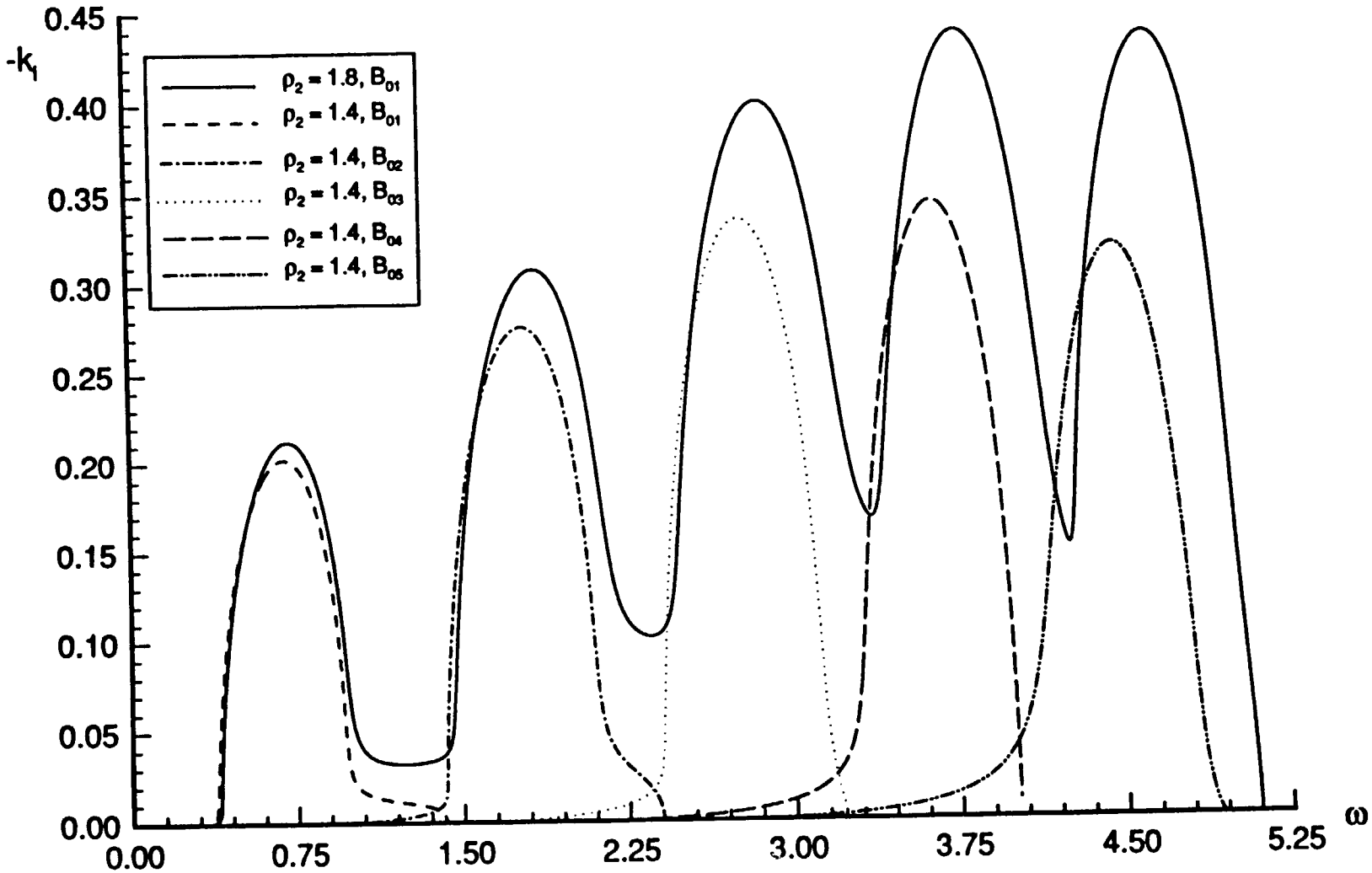
-k_i
0.45
0.40
0.35
0.30
0.25
0.20
0.15
0.10
0.05
0.00
0.00
0.75
1.50
2.25
3.00
3.75
4.50
5.25
ω
ρ2 = 1.8, B01
ρ2 = 1.4, B01
ρ2 = 1.4, B02
ρ2 = 1.4, B03
ρ2 = 1.4, B04
ρ2 = 1.4, B05

Figure 17a

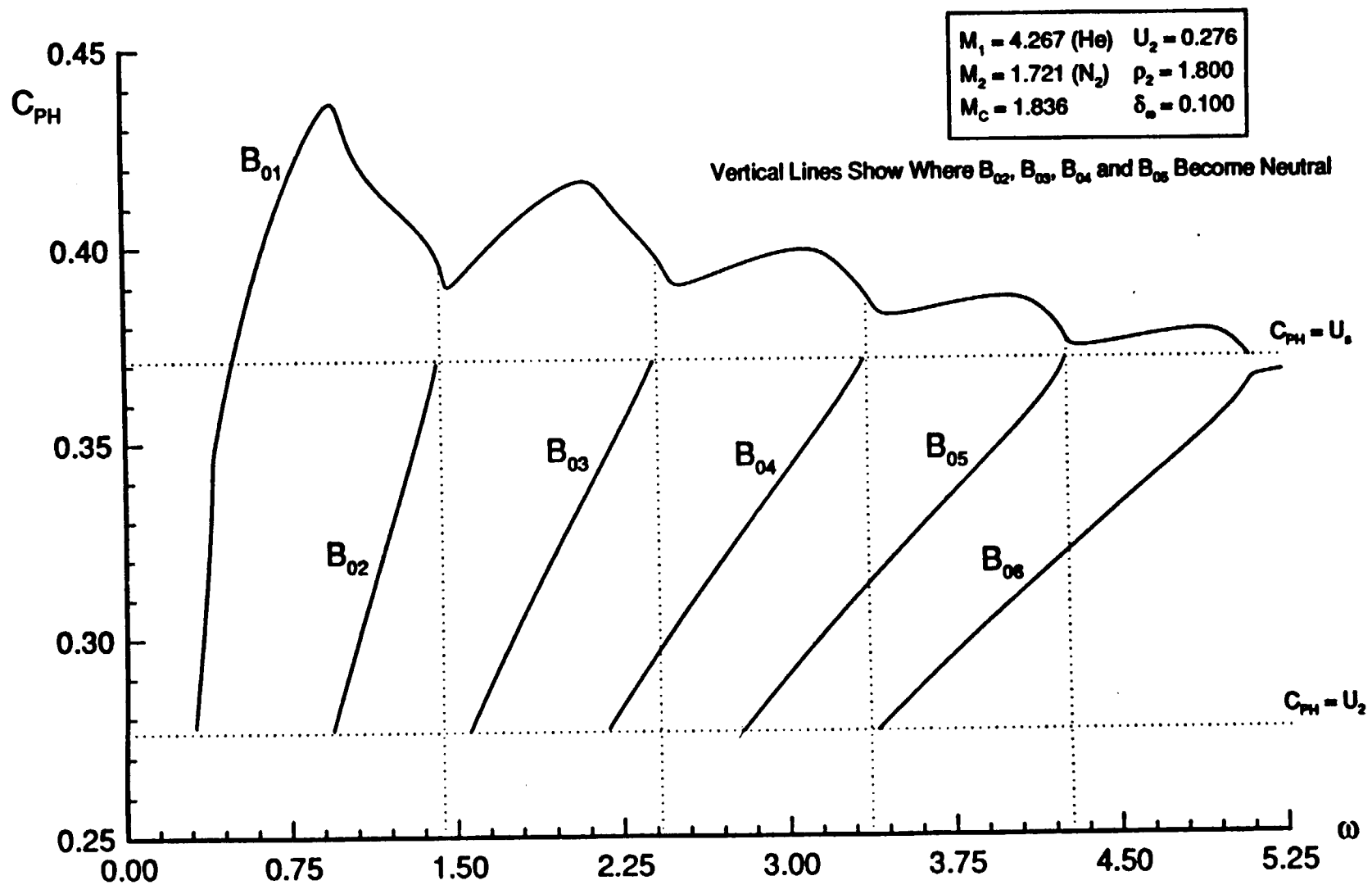
$M_1 = 4.267$ (He) $U_2 = 0.276$
$M_2 = 1.721$ (N_2) $\rho_2 = 1.800$
$M_C = 1.836$ $\delta_\infty = 0.100$
Vertical Lines Show Where B_{02}, B_{03}, B_{04} and B_{05} Become Neutral
C_{PH}
0.45
0.40
0.35
0.30
0.25
B_{01}
B_{02}
B_{03}
B_{04}
B_{05}
B_{06}
$C_{PH} = U_\infty$
$C_{PH} = U_2$
0.00
0.75
1.50
2.25
3.00
3.75
4.50
5.25
ω

Figure 17b

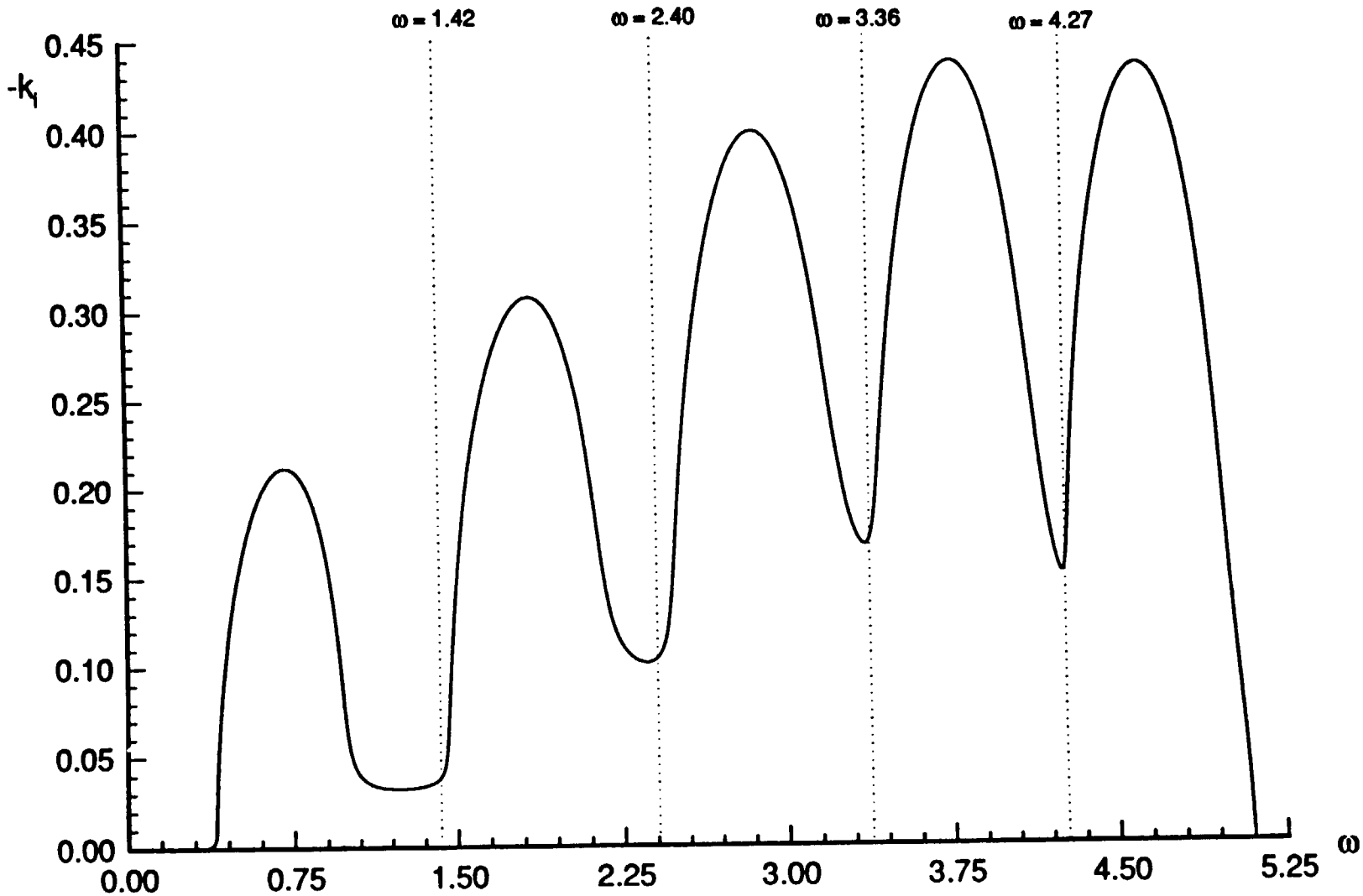
ω = 1.42
ω = 2.40
ω = 3.36
ω = 4.27
-k_i
0.45
0.40
0.35
0.30
0.25
0.20
0.15
0.10
0.05
0.00
0.00
0.75
1.50
2.25
3.00
3.75
4.50
5.25
ω

Figure 18

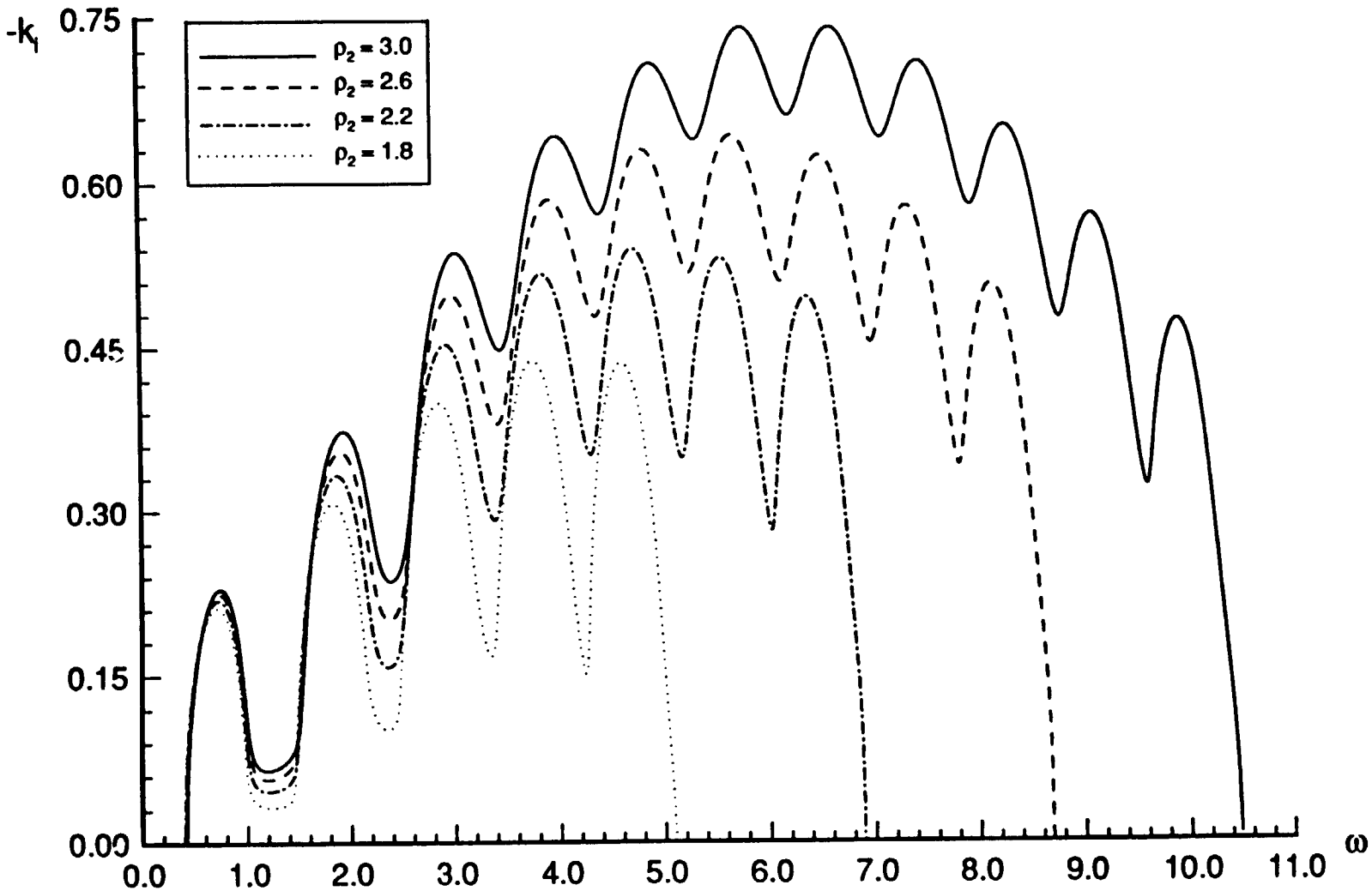
-k_i
0.75
0.60
0.45
0.30
0.15
0.00
ρ2 = 3.0
ρ2 = 2.6
ρ2 = 2.2
ρ2 = 1.8
0.0
1.0
2.0
3.0
4.0
5.0
6.0
7.0
8.0
9.0
10.0
11.0
ω

Figure 19

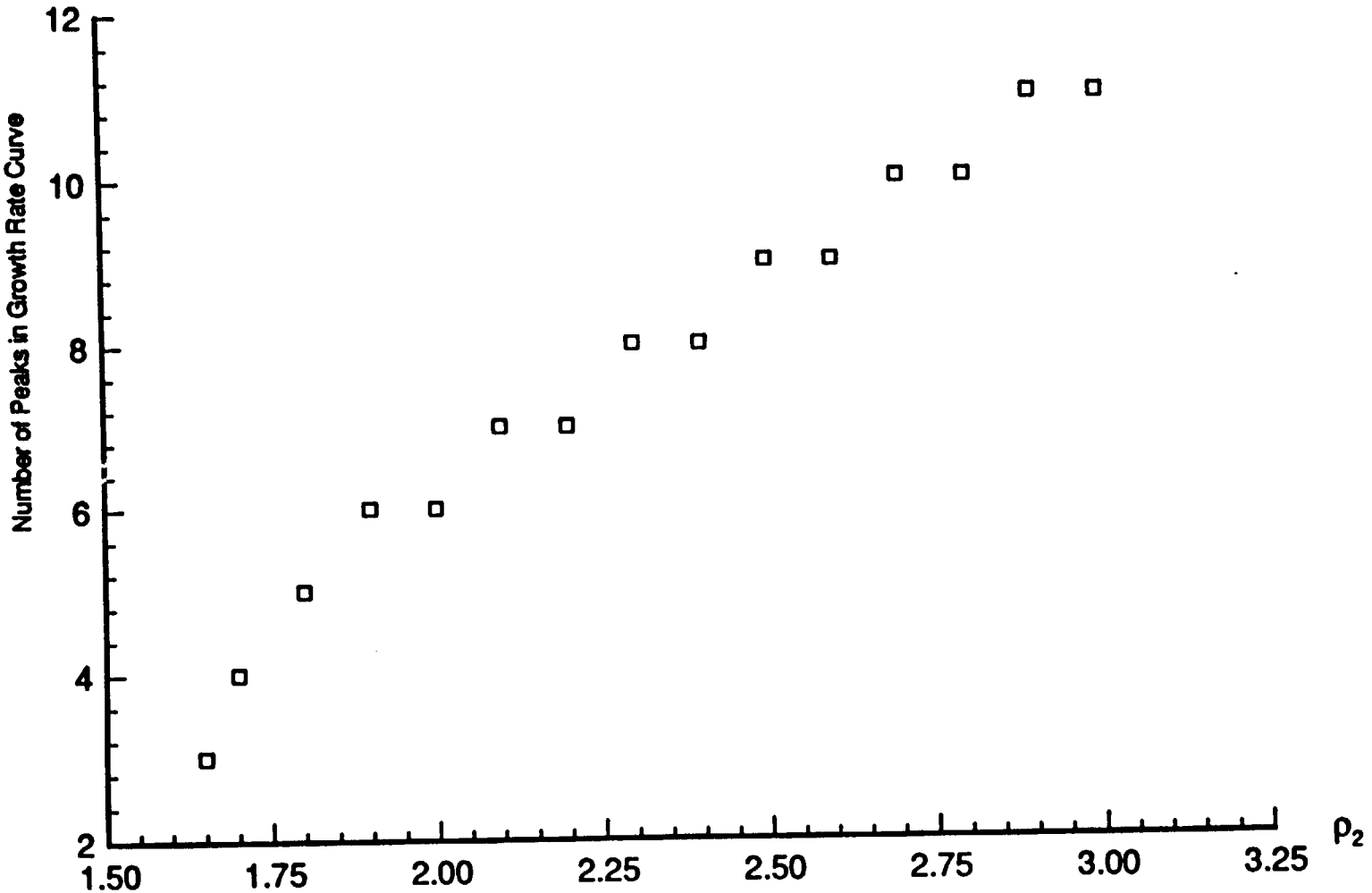
Number of Peaks in Growth Rate Curve
12
10
8
6
4
2
1.50
1.75
2.00
2.25
2.50
2.75
3.00
3.25
ρ_2

Figure 20

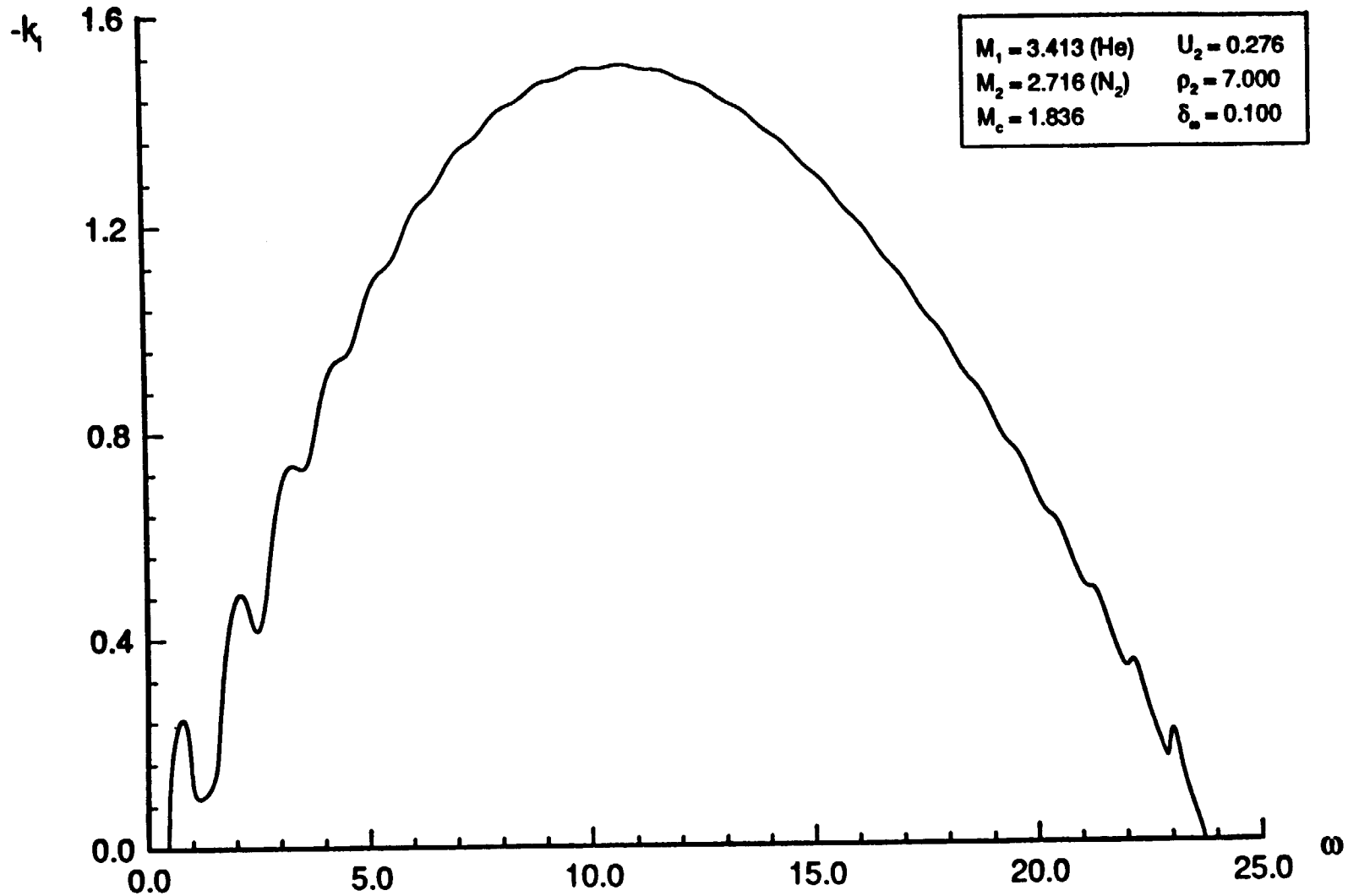
-k_i
1.6
1.2
0.8
0.4
0.0
0.0
5.0
10.0
15.0
20.0
25.0
ω
M_1 = 3.413 (He)
U_2 = 0.276
M_2 = 2.716 (N_2)
ρ_2 = 7.000
M_c = 1.836
δ_m = 0.100

Figure 21

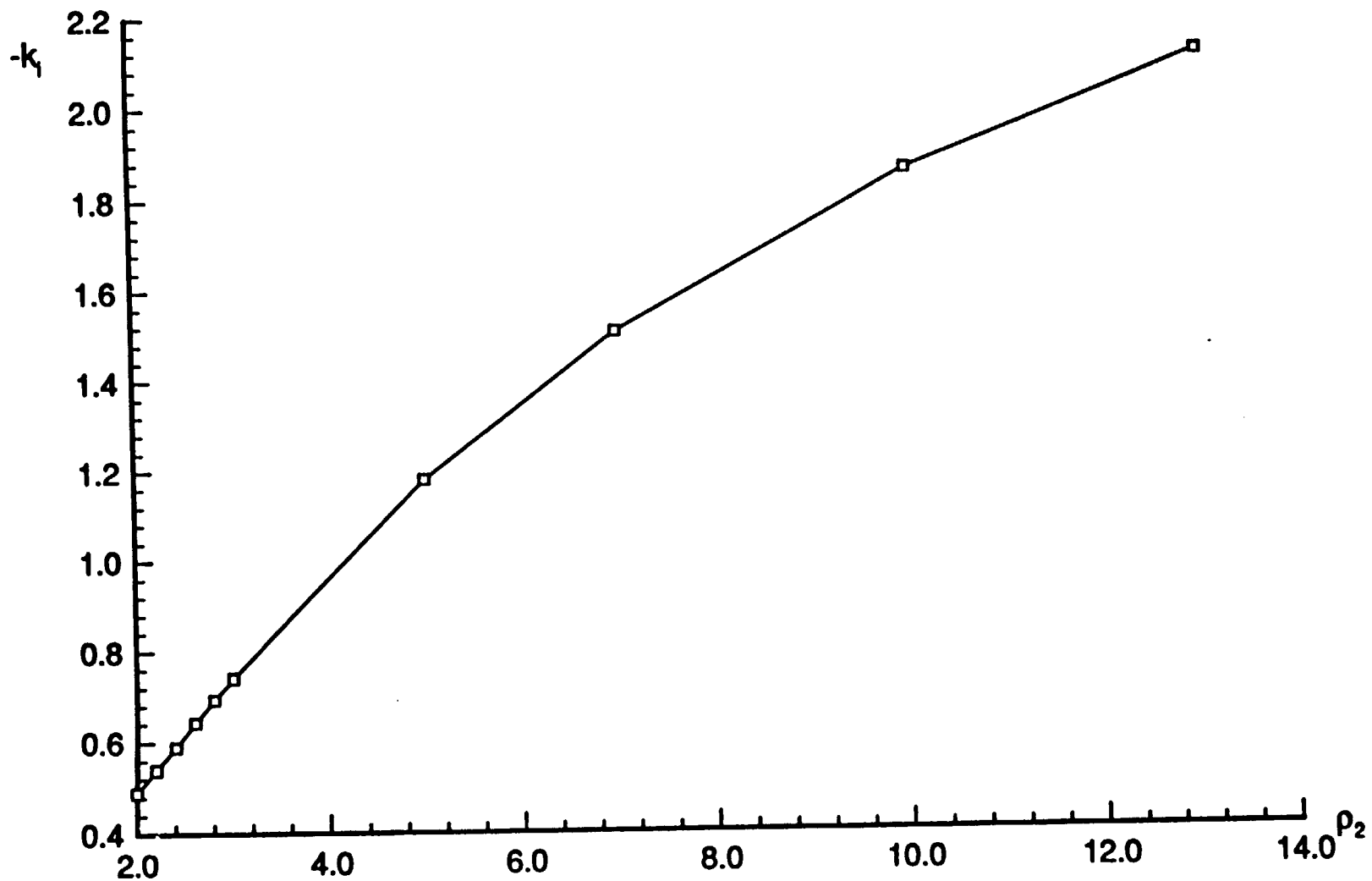

Figure 22

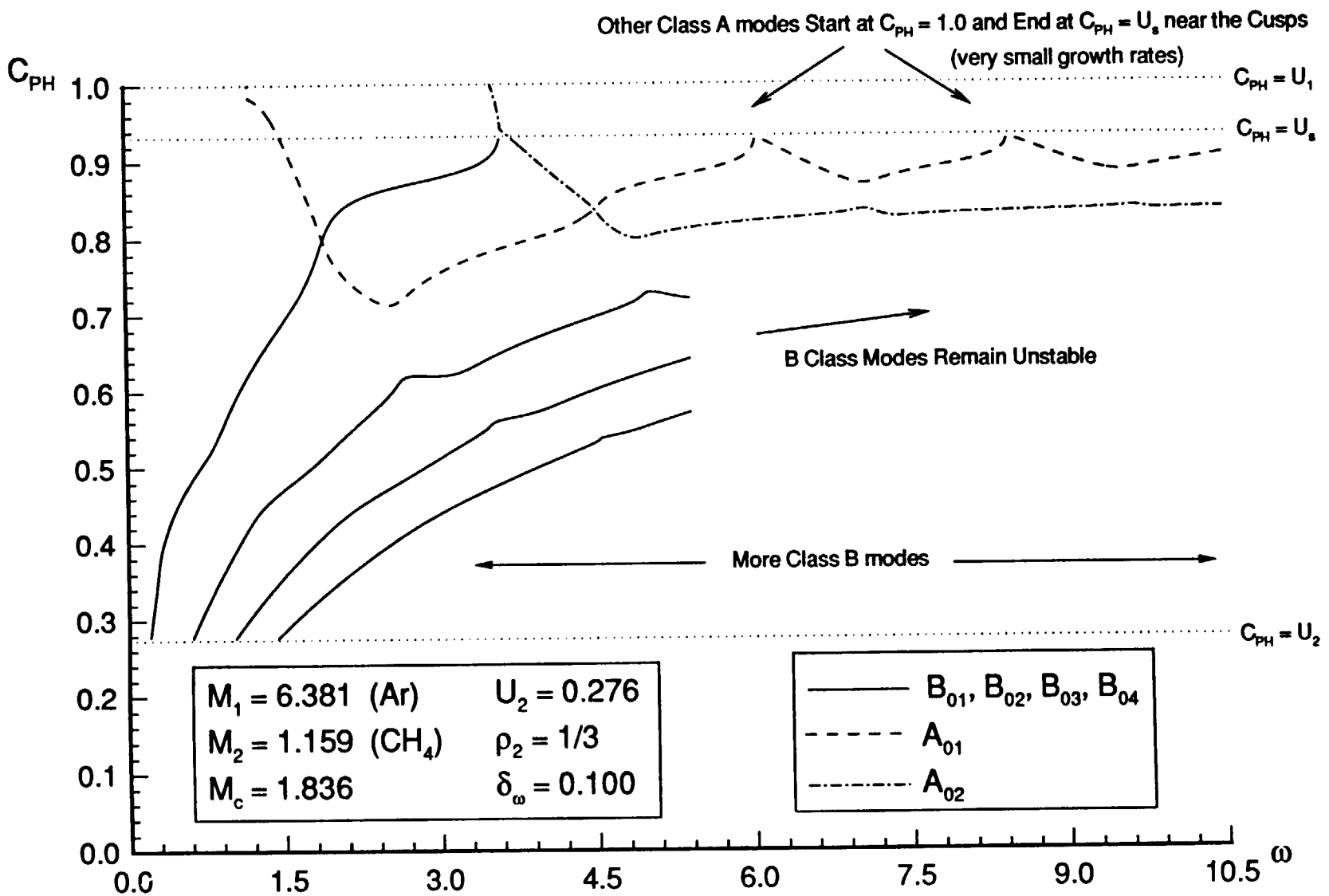
Other Class A modes Start at C_{PH} = 1.0 and End at C_{PH} = U_s near the Cusps
(very small growth rates)
C_{PH}
C_{PH} = U_1
C_{PH} = U_s
B Class Modes Remain Unstable
More Class B modes
C_{PH} = U_2
M_1 = 6.381 (Ar)
M_2 = 1.159 (CH_4)
M_c = 1.836
U_2 = 0.276
ρ_2 = 1/3
δ_ω = 0.100
B_{01}, B_{02}, B_{03}, B_{04}
A_{01}
A_{02}
1.0
0.9
0.8
0.7
0.6
0.5
0.4
0.3
0.2
0.1
0.0
0.0
1.5
3.0
4.5
6.0
7.5
9.0
10.5
ω

Figure 23a

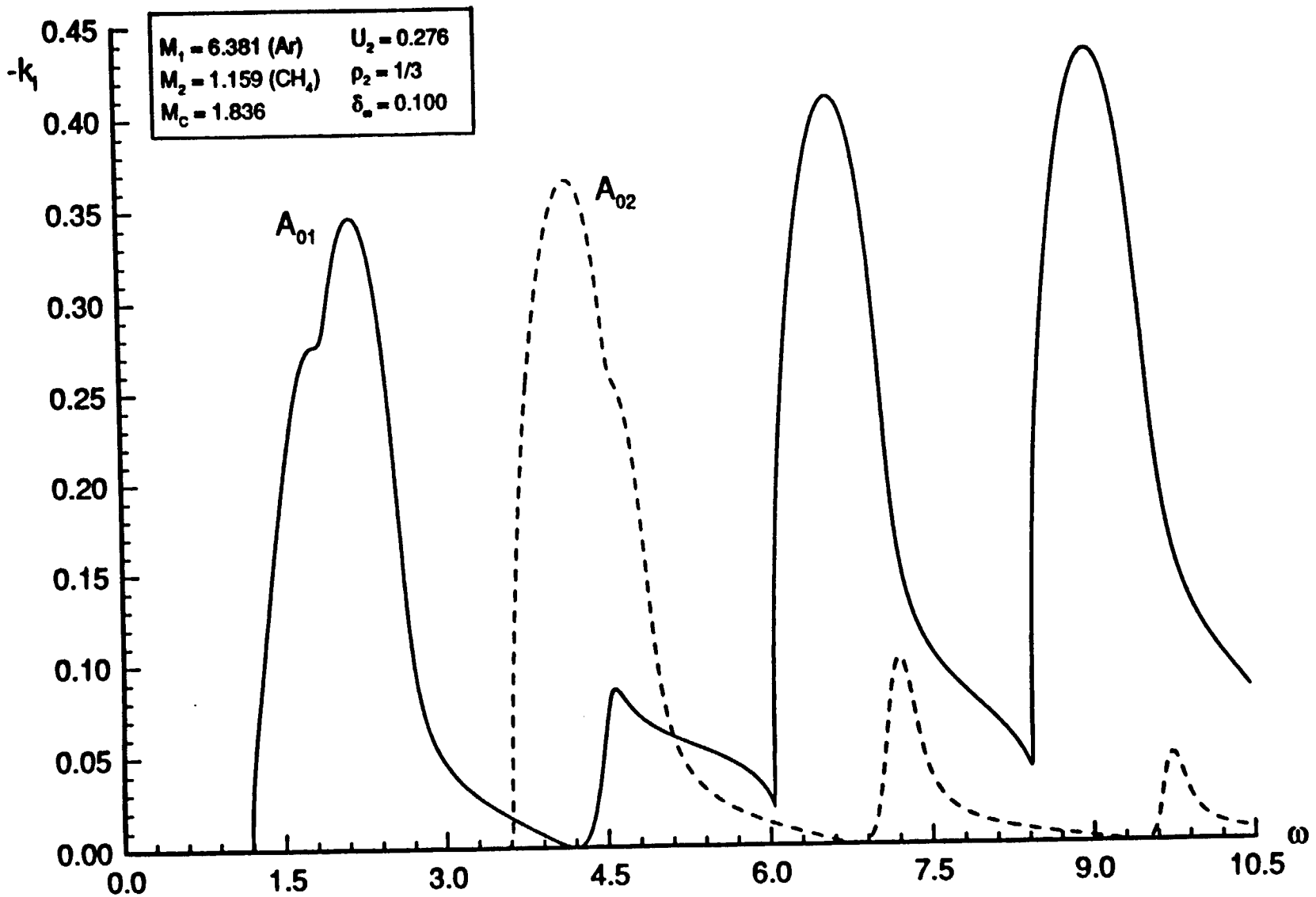
$M_1 = 6.381$ (Ar)
$M_2 = 1.159$ (CH_4)
$M_C = 1.836$
$U_2 = 0.276$
$\rho_2 = 1/3$
$\delta_\infty = 0.100$
$-k_1$
A_{01}
A_{02}
ω
0.45
0.40
0.35
0.30
0.25
0.20
0.15
0.10
0.05
0.00
0.0
1.5
3.0
4.5
6.0
7.5
9.0
10.5

Figure 23b

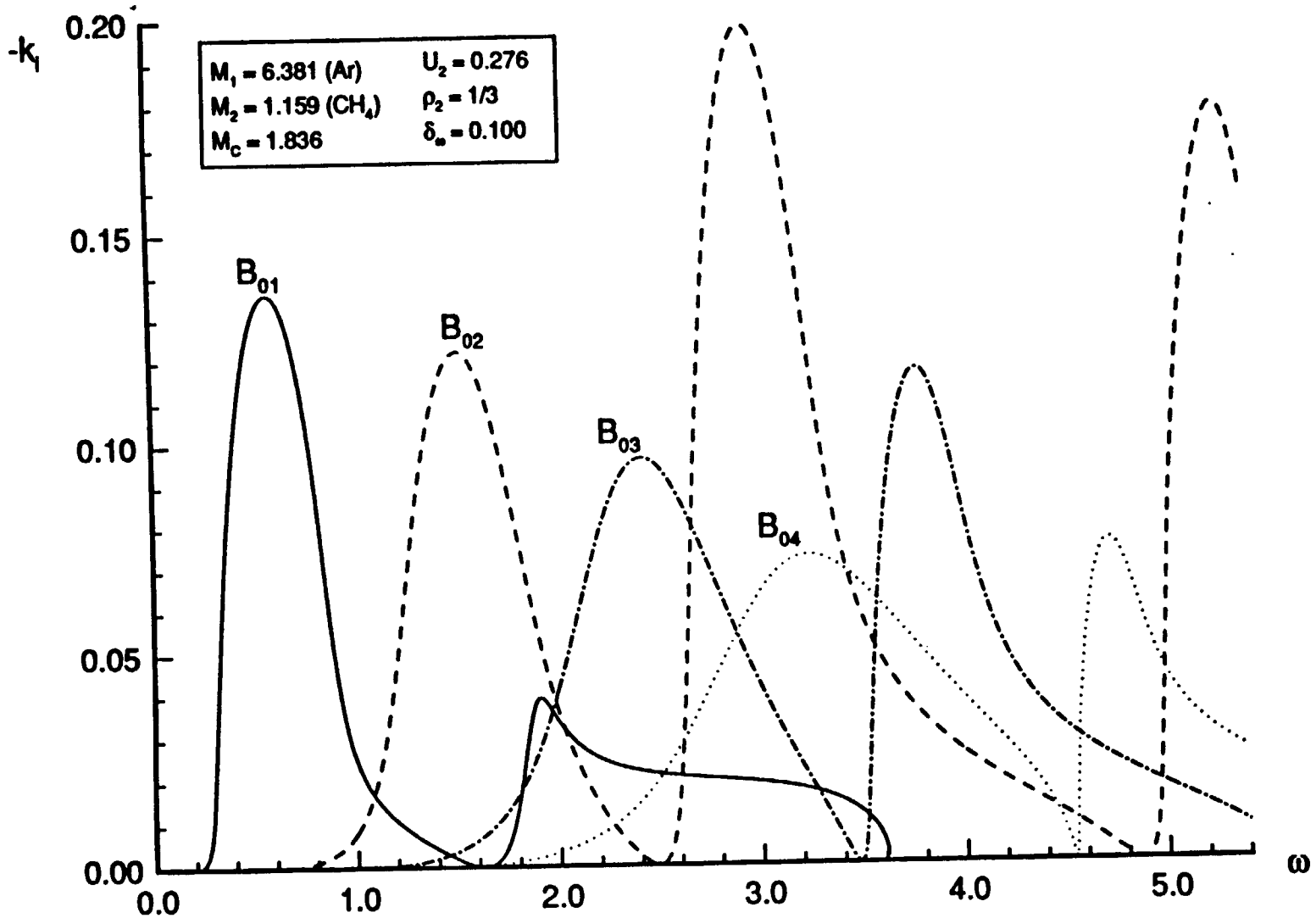
-k_i
0.20
0.15
0.10
0.05
0.00
0.0
1.0
2.0
3.0
4.0
5.0
ω
M_1 = 6.381 (Ar)
M_2 = 1.159 (CH_4)
M_c = 1.836
U_2 = 0.276
ρ_2 = 1/3
δ_∞ = 0.100
B_01
B_02
B_03
B_04

Figure 24

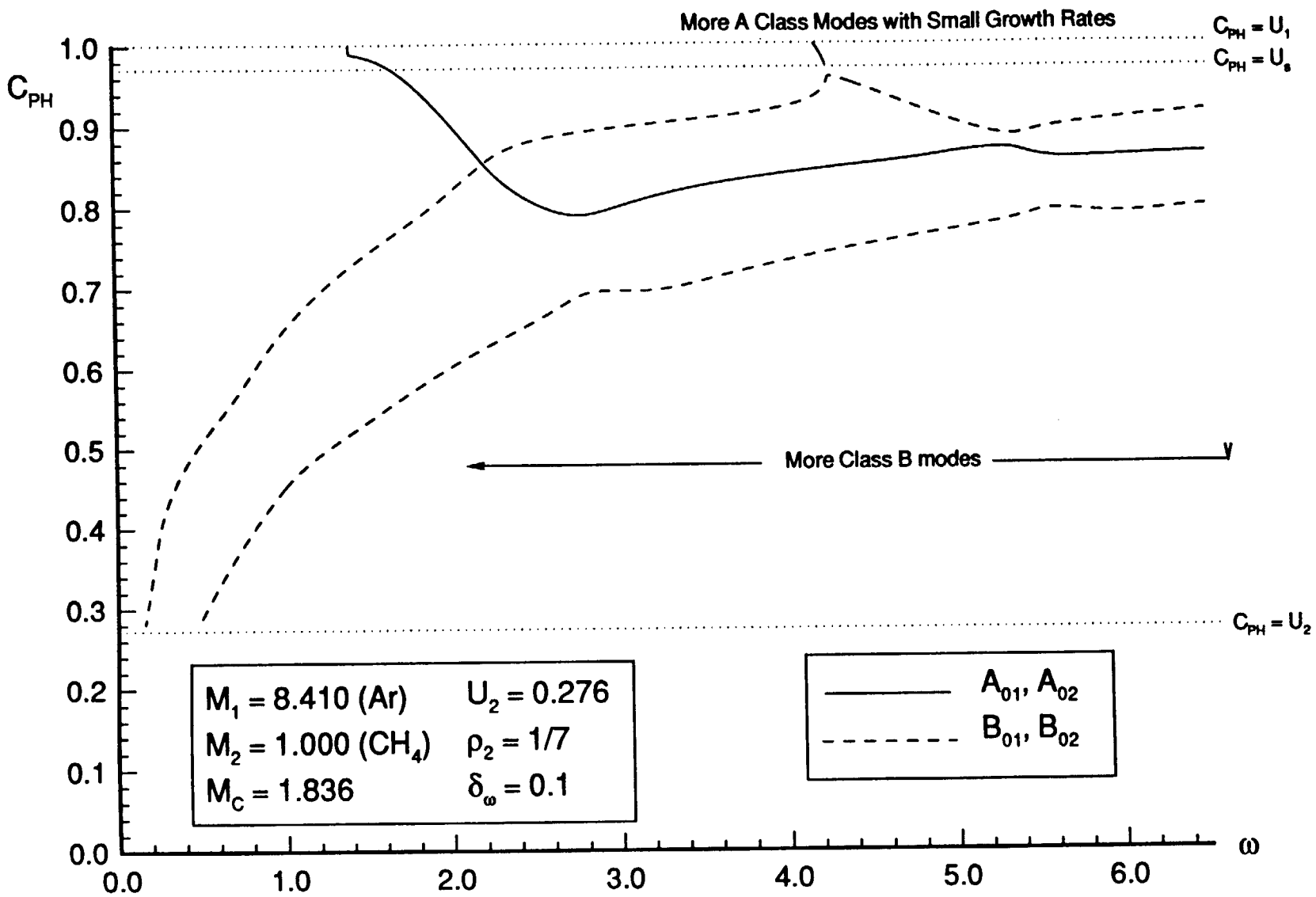
More A Class Modes with Small Growth Rates
$C_{PH} = U_1$
$C_{PH} = U_s$
C_{PH}
1.0
0.9
0.8
0.7
0.6
0.5
0.4
0.3
0.2
0.1
0.0
More Class B modes
$C_{PH} = U_2$
$M_1 = 8.410$ (Ar)
$U_2 = 0.276$
$M_2 = 1.000$ (CH_4)
$\rho_2 = 1/7$
$M_C = 1.836$
$\delta_\omega = 0.1$
A_{01}, A_{02}
B_{01}, B_{02}
0.0
1.0
2.0
3.0
4.0
5.0
6.0
ω

Figure 25

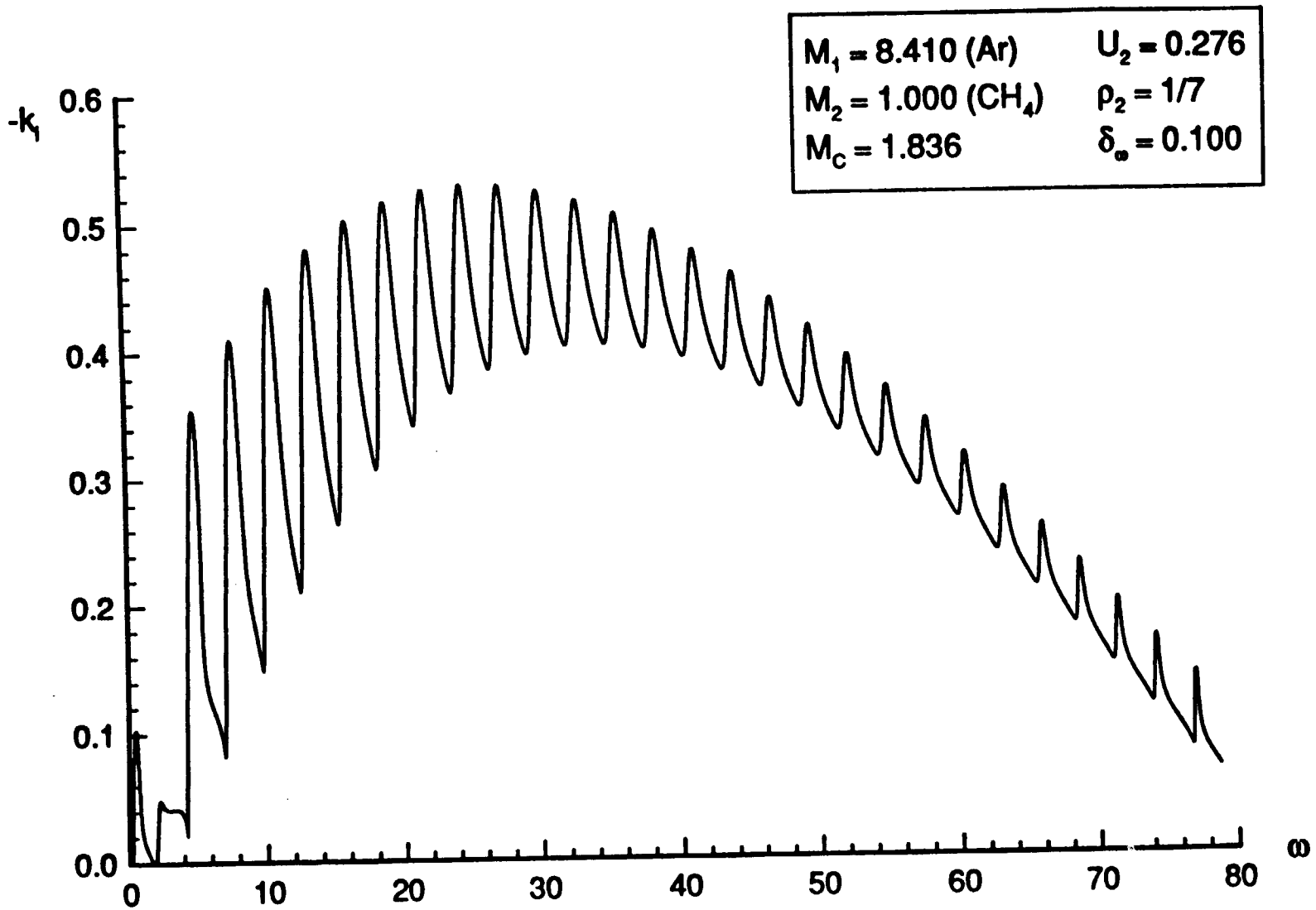
$M_1 = 8.410$ (Ar)
$M_2 = 1.000$ (CH_4)
$M_C = 1.836$
$U_2 = 0.276$
$\rho_2 = 1/7$
$\delta_\infty = 0.100$
$-k_i$
0.6
0.5
0.4
0.3
0.2
0.1
0.0
0
10
20
30
40
50
60
70
80
ω